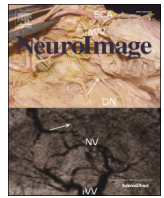




Contents lists available at ScienceDirect

NeuroImage

journal homepage: [www.elsevier.com/locate/ynimg](http://www.elsevier.com/locate/ynimg)

## Source-space ICA for EEG source separation, localization, and time-course reconstruction

Yaqub Jonmohamadi <sup>a,b,\*</sup>, Govinda Poudel <sup>b,c,d</sup>, Carrie Innes <sup>b,e,f</sup>, Richard Jones <sup>a,b,e,f</sup>

<sup>a</sup> Department of Medicine, University of Otago, Christchurch, New Zealand

<sup>b</sup> New Zealand Brain Research Institute, Christchurch, New Zealand

<sup>c</sup> Monash Biomedical Imaging, Monash University, Melbourne, Australia

<sup>d</sup> School of Psychological Sciences, Monash University, Clayton, Victoria, Australia

<sup>e</sup> Department of Electrical and Computer Engineering, University of Canterbury, Christchurch, New Zealand

<sup>f</sup> Department of Medical Physics and Bioengineering, Christchurch Hospital, Christchurch, New Zealand

### ARTICLE INFO

#### Article history:

Accepted 25 July 2014

Available online xxxx

#### Keywords:

Beamformer

EEG

Independent component analysis

Localization

Time-course reconstruction

### ABSTRACT

We propose source-space independent component analysis (ICA) for separation, tomography, and time-course reconstruction of EEG and MEG source signals. Source-space ICA is based on the application of singular value decomposition and ICA on the neuroelectrical signals from all brain voxels obtained post minimum-variance beamforming of sensor-space EEG or MEG. We describe the theoretical background and equations, then evaluate the performance of this technique in several different situations, including weak sources, bilateral correlated sources, multiple sources, and cluster sources. In this approach, tomographic maps of sources are obtained by back-projection of the ICA mixing coefficients into the source-space (3-D brain template). The advantages of source-space ICA over the popular alternative approaches of sensor-space ICA together with dipole fitting and power mapping via minimum-variance beamforming are demonstrated. Simulated EEG data were produced by forward head modeling to project the simulated sources onto scalp sensors, then superimposed on real EEG background. To illustrate the application of source-space ICA to real EEG source reconstruction, we show the localization and time-course reconstruction of visual evoked potentials. Source-space ICA is superior to the minimum-variance beamforming in the reconstruction of multiple weak and strong sources, as ICA allows weak sources to be identified and reconstructed in the presence of stronger sources. Source-space ICA is also superior to sensor-space ICA on accuracy of localization of sources, as source-space ICA applies ICA to the time-courses of voxels reconstructed from minimum-variance beamforming on a 3D scanning grid and these time-courses are optimally unmixed via the beamformer. Each component identified by source-space ICA has its own tomographic map which shows the extent to which each voxel has contributed to that component.

© 2014 Elsevier Inc. All rights reserved.

### Introduction

A substantial advantage of electroencephalography (EEG) and magnetoencephalography (MEG), over other noninvasive functional imaging of the brain, such as functional magnetic resonance imaging (fMRI) and positron emission tomography (PET), is their millisecond temporal resolution. This high temporal resolution provides the opportunity for the study of highly transient brain source activities.

In EEG and MEG, the inverse solution is used to estimate the location of sources and corresponding time-courses. The inverse problem in EEG and MEG, however, is ill-posed as the EEG/MEG scalp sensors are highly outnumbered by the brain source signals.

Several approaches have been proposed for solving the inverse problem including dipole fitting (Mosher et al., 1992; Sarvas, 1987; Uutela et al., 1983), minimum-norm spatial filters (Dale et al., 2000; Hämäläinen and Ilmoniemi, 1994; Pascual-Marqui, 2002), and minimum-variance spatial filters (Greenblatt et al., 2005; Robinson and Vrba, 1998; Sekihara et al., 2001; Van Veen et al., 1997). Dipole fitting is a popular technique which assumes that a predefined number of dipoles have generated the given EEG/MEG segment. The main limitation of this technique is that an arbitrary number of sources must be specified in advance. In addition, dipole fitting finds a single point for each brain source and is unable to produce a tomographic map. Minimum-norm based spatial filters, such as the original minimum-norm filter (Hämäläinen and Ilmoniemi, 1994) and standardized low resolution brain electromagnetic tomography (sLORETA) (Pascual-Marqui, 2002), produce a tomographic map for the whole brain for a given MEG/EEG epoch and do not require prior knowledge of the number of brain sources. Minimum-variance spatial filters, such as the

\* Corresponding author at: New Zealand Brain Research Institute, 66 Stewart Street, Christchurch 8011, New Zealand.

E-mail address: [jonya247@student.otago.ac.nz](mailto:jonya247@student.otago.ac.nz) (Y. Jonmohamadi).

adaptive minimum variance beamformers (Robinson and Vrba, 1998; Sekihara et al., 2001; Van Veen et al., 1997), scan the whole brain (source-space) voxel by voxel and estimate the power of each voxel for a given epoch to produce a tomographic map. Minimum-variance beamformers have been shown to have a higher spatial resolution than minimum-norm based filters and can reconstruct signal sources with a small signal-to-noise-ratio (SNR) (Jonmohamadi et al., 2014a; Sekihara et al., 2005).

The recently proposed Champagne algorithm (Owen et al., 2012; Wipf et al., 2009, 2010) has shown improvement over other popular source localization algorithms in terms of accuracy, robustness to correlated sources, and computational efficiency. However, in the performance evaluation of Champagne (Owen et al., 2012), there is no example of the reconstruction of weak sources, e.g.,  $\text{SNR} < 1$ . Champagne is dependent on segmentation of the EEG/MEG to pre- and post-stimulus epochs, and performance of Champagne is partly dependent on the orientation of the sources as the performance drops when the orientation of the sources is not known (Owen et al., 2012).

The above-mentioned techniques are based on detecting sources based on measuring the power and, therefore, these techniques may not be able to detect weak sources in the presence of stronger interfering sources. Besides measuring the power of the signals for source localization, the statistical properties of the signals, such as entropy and non-Gaussianity, can be estimated and used as a means to detect and separate source signal time-courses. Independent component analysis (ICA) is a blind source separation (BSS) technique which aims to separate  $P$  mutually statistically independent, zero mean, sources from  $M$  linearly combined signal mixtures (Sanei and Chambers, 2007). In EEG and MEG, ICA has been extensively used for component extraction of event related potentials (ERPs) (Jervis et al., 2007; La Foresta et al., 2009; Makeig et al., 2004; Onton et al., 2006; Ventouras et al., 2010) and for artifact removal (Fatima et al., 2013; Jung et al., 1998, 2000).

In the case of source localization, ICA accompanied with dipole fitting (Makeig et al., 2004) has been applied to localize and reconstruct the time-course of the sources. In this approach, after applying ICA on EEG (sensor-space ICA), dipole fitting is used to localize the identified sensor-space components in the source-space (brain). The limitation of this approach is that dipole fitting does not provide a tomographic map and shows a single point as the location of the generator of the identified sensor-space independent component. In another approach (Ventouras et al., 2010), sLORETA has been applied instead of dipole fitting for the components of sensor-space ICA which can provide the tomographic maps. As a minimum-norm spatial filter, sLORETA has been shown to have low spatial resolution compared to minimum-variance beamformers (Sekihara et al., 2005) and, as will be demonstrated, dipole fitting of sensor-space independent components is not accurate in localization of sources.

We propose source-space ICA for separation, tomography and time-course reconstruction of EEG and MEG source signals (Jonmohamadi et al., 2013), which, similar to minimum-variance beamformers, has a high spatial resolution and, similar to ICA, can separate weak and strong sources and provide a unique spatial signature for every separated source. Source-space ICA applies a vector minimum-variance spatial filter to reconstruct the time-series of the source-space (brain volume) on a 3D scanning grid and then applies singular value decomposition and ICA to separate the sources. This approach does not rely on a known number of sources and their orientations, or pre- and post-stimulus segmentation, but also estimates the orientations of the separated sources. The difference between the popular sensor-space ICA and the proposed source-space ICA is that, in sensor-space ICA, the ICA is applied to the time-courses of the data from actual sensors (scalp EEG/MEG sensors), whereas, in source-space ICA, the ICA is applied to the time-courses of a 3D grid of virtual sensors in the brain (as reconstructed via beamforming). Consequently, the independent components of sensor-space signals have corresponding topographic maps, whereas the

independent components of the source-space signals have corresponding tomographic maps.

In this paper, the performance of source-space ICA in several simulated situations, including single and multiple weak sources, bilateral correlated sources, and cluster sources is evaluated and compared with the beamforming technique and sensor-space ICA/dipole fitting (Makeig et al., 2004). Finally, we demonstrate the source-space ICA approach for source reconstruction of real visual evoked potentials (VEPs). Throughout this paper, plain italics indicate scalars, lower-case boldface italics indicate vectors, and upper-case boldface italics indicate matrices.

## Methods

### Problem formulation

The EEG signal for  $K$  time samples  $\mathbf{B}(t) = [\mathbf{b}(t_1), \mathbf{b}(t_2), \dots, \mathbf{b}(t_K)]^T$ , on  $M$  sensors, at time point  $t$  is

$$\mathbf{b}(t) = \int \mathbf{L}(\mathbf{r})\mathbf{q}(\mathbf{r})s(t, \mathbf{r})d(\mathbf{r}) + \boldsymbol{\eta}(t), \quad (1)$$

and  $\mathbf{L}(\mathbf{r}) = [\mathbf{L}_x(\mathbf{r}), \mathbf{L}_y(\mathbf{r}), \mathbf{L}_z(\mathbf{r})]$  is a  $M \times 3$  lead-field matrix which shows the sensitivity of scalp sensors in three orthogonal directions ( $x, y, z$ ) to the source signal  $s(t, \mathbf{r})$  located at  $\mathbf{r} = [r_x, r_y, r_z]^T$  (mm) with a moment of  $\mathbf{q}(\mathbf{r}) = [q_x(\mathbf{r}), q_y(\mathbf{r}), q_z(\mathbf{r})]^T$  (A·m), and  $\boldsymbol{\eta}(t)$  is the additive noise.

The reconstructed time-course,  $\hat{\mathbf{s}}(t, \mathbf{r}) = [\hat{s}_x(t, \mathbf{r}), \hat{s}_y(t, \mathbf{r}), \hat{s}_z(t, \mathbf{r})]^T$ , for a given location  $\mathbf{r}$  to the vector spatial filter can be written as

$$\hat{\mathbf{s}}(t, \mathbf{r}) = \mathbf{W}^T(\mathbf{r})\mathbf{b}(t), \quad (2)$$

where  $\mathbf{W}(\mathbf{r}) = [\mathbf{w}_x(\mathbf{r}), \mathbf{w}_y(\mathbf{r}), \mathbf{w}_z(\mathbf{r})]$  is a  $M \times 3$  matrix of the vector spatial filter coefficients. One way to obtain a tomographic map for all the brain locations (voxels) for a given EEG/MEG segment, is to measure the power for each voxel

$$\mathbf{p}_\xi(\mathbf{r}) = \mathbf{w}_\xi^T(\mathbf{r})\mathbf{C}\mathbf{w}_\xi(\mathbf{r}) = \langle \hat{\mathbf{s}}_\xi(t, \mathbf{r})^2 \rangle, \quad (3)$$

$\xi \in x, y, z; \mathbf{r} \in \Omega,$

where  $\langle \dots \rangle$  is the ensemble average, and  $\Omega$  is the different location on the scanning grid which covers the whole brain (source-space), and  $\mathbf{C}$  is the covariance matrix

$$\mathbf{C} = \langle \mathbf{b}(t)\mathbf{b}^T(t) \rangle. \quad (4)$$

In Eq. (3), only the dominant sources will be identified for the period that  $\mathbf{C}$  is measured but weaker sources may not be identified due to their small power.

### Beamformer

Beamforming, as a form of spatial filtering, is a popular technique for localization and signal reconstruction of brain sources in EEG and MEG and has been successfully applied (Robinson and Vrba, 1998; Sekihara et al., 2001; Van Veen et al., 1997) and the performances of different beamformers have been evaluated (Greenblatt et al., 2005; Huang et al., 2004; Sekihara et al., 2005). Of the several beamformers, we chose the vector weight-normalized minimum-variance (WNNMV) beamformer, also known as Borgiotti–Kaplan (Sekihara et al., 2001), as it has normalized weight vectors which results in unit noise gain and, hence, the time-courses of all voxels have the same gain. The weight matrix of the vector WNNMV beamformer is

$$\mathbf{W}_{\text{WNNMV}}(\mathbf{r}) = \frac{\mathbf{C}^{-1}\mathbf{L}(\mathbf{r})\mathbf{P}^{-1}(\mathbf{r})}{\sqrt{\mathbf{P}^{-1}(\mathbf{r})\mathbf{Q}(\mathbf{r})\mathbf{P}^{-1}(\mathbf{r})}}$$

where  $\mathbf{P}(\mathbf{r})$  and  $\mathbf{Q}(\mathbf{r})$  are

$$\begin{aligned} \mathbf{P}(\mathbf{r}) &= \mathbf{L}^T(\mathbf{r})\mathbf{C}^{-1}\mathbf{L}(\mathbf{r}) \text{ and} \\ \mathbf{Q}(\mathbf{r}) &= \mathbf{L}^T(\mathbf{r})\mathbf{C}^{-1}\mathbf{L}(\mathbf{r}). \end{aligned} \quad (6)$$

The constraint of the WNMV beamformer ensures that the gain is the same in all locations

$$\mathbf{W}_{\text{WNMV}}^T(\mathbf{r})\mathbf{W}_{\text{WNMV}}(\mathbf{r}) = \mathbf{I}, \quad (7)$$

where  $\mathbf{I}$  is the identity matrix.

The magnitude time-series of each voxel via the WNMV beamformer is obtained via

$$\begin{aligned} |\hat{s}(t, \mathbf{r}_b)| &= \sqrt{\text{tr}\{\mathbf{W}^T(\mathbf{r}_b)\mathbf{b}(t)\mathbf{b}^T(t)\mathbf{W}(\mathbf{r}_b)\}} \\ &= \sqrt{\hat{s}_x^2(t, \mathbf{r}) + \hat{s}_y^2(t, \mathbf{r}) + \hat{s}_z^2(t, \mathbf{r})}. \end{aligned} \quad (8)$$

For source-space power measurement via beamforming, the mean power of the source-space over an EEG epoch is estimated via

$$\langle |\hat{s}(t, \mathbf{r}_b)| \rangle = \sqrt{\langle \text{tr}\{\mathbf{W}^T(\mathbf{r}_b)\mathbf{b}(t)\mathbf{b}^T(t)\mathbf{W}(\mathbf{r}_b)\} \rangle}. \quad (9)$$

### Source-space ICA

Source-space ICA comprises the following basic steps:

- Divide the brain (source-space) via a 3D scanning grid into  $N$  voxels.
- Apply the vector WNMV beamformer to sensor-space data to reconstruct the 3 orthogonal time-series of each voxel in the source-space and store it in the source-space data matrix (rows of the data matrix are the time-series of each voxel).
- Determine the rank of the source-space data matrix.
- Apply SVD to the source-space data matrix to reduce the size of the matrix to its rank.
- Separate the temporal and spatial subspaces of the reduced data matrix.
- Apply ICA to the temporal subspace.
- Use the mixing matrix of the ICA to the spatial subspace to produce tomographic maps of the identified components.

The block diagram of source-space ICA is shown in Fig. 1.

Source-space ICA is based on the application of ICA as a BSS technique on the reconstructed time-courses of all brain voxels via the vector WNMV beamformer. Since the reconstructed time-course for a given location is the source signal at that location partially mixed with interfering sources (i.e.,  $\hat{\mathbf{s}}(t, \mathbf{r}) \neq \mathbf{s}(t, \mathbf{r})$ ), ICA can be applied to separate the statistically independent source signals. The reconstructed source-space data matrix  $\hat{\mathbf{S}} \in \mathcal{R}^{(3N \times K)}$  for all  $N$  voxels and time samples  $K$  is

$$\hat{\mathbf{S}} = \begin{pmatrix} \hat{s}_x(t_1, \mathbf{r}_1) \hat{s}_x(t_2, \mathbf{r}_1) \dots \hat{s}_x(t_K, \mathbf{r}_1) \\ \hat{s}_y(t_1, \mathbf{r}_1) \hat{s}_y(t_2, \mathbf{r}_1) \dots \hat{s}_y(t_K, \mathbf{r}_1) \\ \hat{s}_z(t_1, \mathbf{r}_1) \hat{s}_z(t_2, \mathbf{r}_1) \dots \hat{s}_z(t_K, \mathbf{r}_1) \\ \hat{s}_x(t_1, \mathbf{r}_2) \hat{s}_x(t_2, \mathbf{r}_2) \dots \hat{s}_x(t_K, \mathbf{r}_2) \\ \hat{s}_y(t_1, \mathbf{r}_2) \hat{s}_y(t_2, \mathbf{r}_2) \dots \hat{s}_y(t_K, \mathbf{r}_2) \\ \hat{s}_z(t_1, \mathbf{r}_2) \hat{s}_z(t_2, \mathbf{r}_2) \dots \hat{s}_z(t_K, \mathbf{r}_2) \\ \vdots \\ \hat{s}_x(t_1, \mathbf{r}_N) \hat{s}_x(t_2, \mathbf{r}_N) \dots \hat{s}_x(t_K, \mathbf{r}_N) \\ \hat{s}_y(t_1, \mathbf{r}_N) \hat{s}_y(t_2, \mathbf{r}_N) \dots \hat{s}_y(t_K, \mathbf{r}_N) \\ \hat{s}_z(t_1, \mathbf{r}_N) \hat{s}_z(t_2, \mathbf{r}_N) \dots \hat{s}_z(t_K, \mathbf{r}_N) \end{pmatrix}. \quad (10)$$

Since the rank of the data matrix  $\hat{\mathbf{S}}$  is  $\leq M$ , applying ICA to  $\hat{\mathbf{S}}$  is an undercomplete ICA problem where the number of the signal mixtures  $3N \geq \text{rank}(\hat{\mathbf{S}})$  and ICA will not provide a correct estimation of the

sources. In addition, ICA algorithms are computationally demanding and, therefore, SVD is needed for dimensional reduction of the source-space data matrix  $\hat{\mathbf{S}}$ . Via SVD,

$$\hat{\mathbf{S}} = \mathbf{U}\mathbf{\Sigma}\mathbf{V}^T, \quad (11)$$

where  $\mathbf{U}$  and  $\mathbf{V}^T$  are  $3N \times 3N$  and  $K \times K$  unitary matrices respectively and  $\mathbf{\Sigma}$  is a  $3N \times K$  diagonal matrix with its diagonal elements being the singular values on descending order. For dimensional reduction,  $\hat{\mathbf{S}}$  is decomposed as

$$\begin{aligned} \hat{\mathbf{S}} &= [\mathbf{U}_D \mathbf{U}_{UD}] \begin{bmatrix} \mathbf{\Sigma}_D & \mathbf{0} \\ \mathbf{0} & \mathbf{\Sigma}_{UD} \end{bmatrix} [\mathbf{V}_D^T \mathbf{V}_{UD}^T] \\ &= \mathbf{U}_D \mathbf{\Sigma}_D \mathbf{V}_D^T + \mathbf{U}_{UD} \mathbf{\Sigma}_{UD} \mathbf{V}_{UD}^T = \hat{\mathbf{S}}_D + \hat{\mathbf{S}}_{UD}, \end{aligned} \quad (12)$$

where  $\hat{\mathbf{S}}_D$  is the desired subspace of the source-space data matrix and  $\hat{\mathbf{S}}_{UD}$  is the undesired subspace containing noise only. Therefore,  $\mathbf{\Sigma}_D$  contains the first  $M'$  singular values and  $M' \leq M$ . In the case of high density EEG, e.g.,  $M = 512$ , a smaller number should be considered for  $M'$ , dependent on the length of the EEG measurement. Therefore, to define  $M'$ , the rank test for the data matrix was used,  $M' = \text{rank}(\hat{\mathbf{S}})$ . By appli-

cation of ICA on the temporal subspace,  $\mathbf{Y} = \mathbf{\Sigma}_D \mathbf{V}_D^T$ ,  $\mathbf{Y} \in \mathcal{R}^{(M' \times K)}$ , we can estimate the independent components and the unmixing matrix via ICA  $\bar{\mathbf{S}} = \mathbf{H}\mathbf{Y}$ ,

$$\bar{\mathbf{S}} = \mathbf{H}\mathbf{Y}, \quad (13)$$

where  $\mathbf{H} \in \mathcal{R}^{(M' \times M')}$  is the unmixing matrix,  $\bar{\mathbf{S}}$  is the matrix of independent components and the  $i$ th row of  $\bar{\mathbf{S}} = [\bar{\mathbf{s}}_1, \bar{\mathbf{s}}_2, \dots, \bar{\mathbf{s}}_{M'}]^T$  is the time-series of the  $i$ th independent component. The tomographic maps of  $M'$  identified components in  $\bar{\mathbf{S}}$  can be obtained by multiplication of the spatial subspace  $\mathbf{U}_D \in \mathcal{R}^{(3N \times M')}$  to the mixing matrix  $\mathbf{H}^{-1}$

$$\mathbf{G} = \mathbf{U}_D \mathbf{H}^{-1}, \quad (14)$$

where the  $i$ th column of  $\mathbf{G} = [\mathbf{g}_1, \mathbf{g}_2, \dots, \mathbf{g}_{M'}] \in \mathcal{R}^{(3N \times M')}$  shows the 3D map for the  $i$ th row of  $\bar{\mathbf{S}}$ . However, for each location  $\mathbf{r}$ , the column vector  $\mathbf{g}_i$  has 3 coefficients (x, y, z) corresponding to the vector beamformer

$$\mathbf{g}_i = [g_{ix}(\mathbf{r}_1), g_{iy}(\mathbf{r}_1), g_{iz}(\mathbf{r}_1), g_{ix}(\mathbf{r}_2), g_{iy}(\mathbf{r}_2), g_{iz}(\mathbf{r}_2), \dots, g_{iz}(\mathbf{r}_N)]^T, \quad (15)$$

$$i = 1, 2, \dots, M',$$

to obtain a single value for each location, vector addition is applied to the 3 orthogonal values

$$|g_i(\mathbf{r}_n)| = \sqrt{g_{ix}^2(\mathbf{r}_n) + g_{iy}^2(\mathbf{r}_n) + g_{iz}^2(\mathbf{r}_n)} \quad n=1, 2, \dots, \quad (16)$$

and

$$\mathbf{g}_i[|g_i(\mathbf{r}_1)|, |g_i(\mathbf{r}_2)|, \dots, |g_i(\mathbf{r}_N)|]^T, i=1, 2, \dots, M'. \quad (17)$$

The tomographic map of the  $i$ th component in  $\bar{\mathbf{S}}$ , i.e.,  $\bar{\mathbf{s}}_i$ , is obtained by projecting the vector  $\mathbf{g}_i$  to the 3D scanning grid.

The location of the voxel in the source-space with maximum intensity for the  $i$ th component is

$$\mathbf{r}_{\max} = \arg \max_{\mathbf{r}_n} (|g_i(\mathbf{r}_n)|), n = 1, 2, \dots, N. \quad (18)$$

The normalized orientation of the  $i$ th component at its focal location  $\mathbf{r}_{\max}$  is

$$\bar{\mathbf{q}}_i(\mathbf{r}_{\max}) = \left[ \frac{g_{ix}(\mathbf{r}_{\max})}{|g_i(\mathbf{r}_{\max})|}, \frac{g_{iy}(\mathbf{r}_{\max})}{|g_i(\mathbf{r}_{\max})|}, \frac{g_{iz}(\mathbf{r}_{\max})}{|g_i(\mathbf{r}_{\max})|} \right]^T. \quad (19)$$

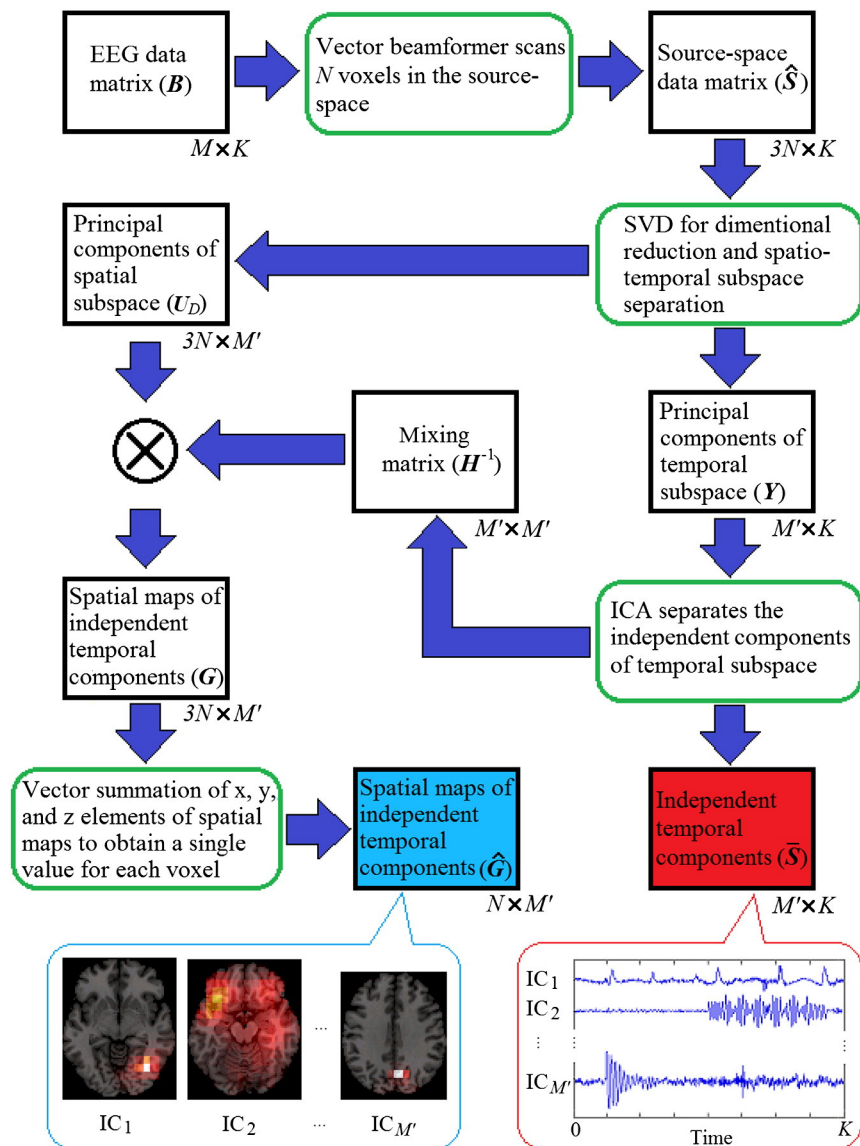


**Fig. 1.** Block diagram of source-space ICA. Each rectangle is a matrix of data. The red and blue rectangles contain the final results for temporal and spatial information. The rows of the red rectangle are independent temporal components, unmixed by ICA, and their 3D maps are columns of the blue rectangle, i.e., the  $i$ th column of the blue rectangle shows the 3D map of the  $i$ th row of the red rectangle.  $N$ : number of voxels,  $M$ : number of EEG sensors,  $M'$ : rank of the source-space data matrix ( $M' \leq M$ ),  $K$ : number of time samples.

Although,  $\mathbf{r}_{max}$  has been used to identify the orientation of the component at the focal point, in the case of network sources, Eq. (19) can be applied to any  $\mathbf{r}_n$  which has a high  $|g(\mathbf{r}_n)|$  value or, in the case of cluster sources, the orientation can be obtained by averaging the orientations of all the voxels in the cluster or just by considering the center of the cluster to obtain the orientation of the source.

### Computer simulations

The background EEG for simulated sources was real EEG from a healthy subject, recorded during the resting state. The 64-channel 10–20 system was used for positioning of the EEG sensors and the EEG was sampled at 250 Hz and band-pass filtered at 1–45 Hz. Montreal Neurological Institute (MNI) coordinates (Bush and Luu, 2000) were used to describe the locations in the brain. The boundary element method (BEM) model of the head (Oostendorp and van Oosterom, 1989) with 3 layers and a conductivity ratio of skull to soft tissue of 0.0125, obtained from the average MNI-template brain and implemented via the FieldTrip toolbox (Oostenveld et al., 2011), was used to calculate the

lead-field matrix. The x, y, and z axes are shown in Fig. 2. The EEGLAB toolbox (Delorme and Makeig, 2004) was used for the ICA algorithm (infomax Bell and Sejnowski, 1995).

To compare the performance of source-space ICA with sensor-space ICA and with beamformers, simulated EEG data were synthesized in several situations. The SNR of the simulated sources superimposed on the real EEG was defined as the Frobenius norm of the source signal matrix to that of the real EEG matrix. The SNR of the sources was 0.5 if not mentioned in the simulations. We did not need to reduce the rank of the sensor-data matrix for sensor-space ICA, and the sensor-data matrix was always full rank, as the lengths of the simulated and real EEG were sufficient for this.

The 3D scanning grid divides the brain into 2041 voxels, each of  $10 \times 10 \times 10 \text{ mm}^3$ . Performance was estimated in terms of ability to identify and localize the sources. The quality of the reconstructed time-courses of the simulated sources is also measured in terms of SNR which was measured after fast Fourier transformation of the time-courses and division of the power at the frequency of the source by summation of the power in other frequencies. Localization error

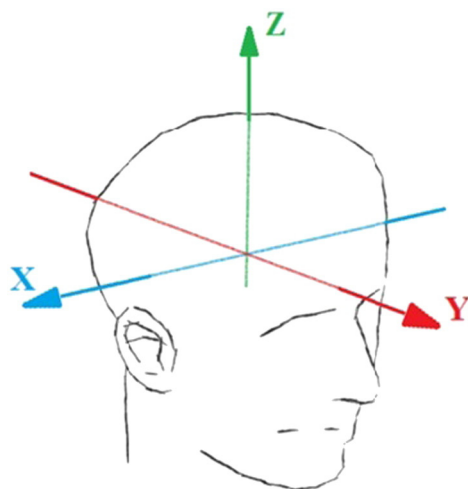


**Fig. 2.** The direction of the x, y, and z axes in the coordinate system used to describe the spatial location of the artificial dipole in the brain. Coordinate [0, 0, 0] is at the anterior commissure and in line with the anterior/posterior commissural line.

(LE) is the distance of the center of voxel with maximum intensity ( $\hat{\mathbf{r}}$ ) to that of the actual location ( $\mathbf{r}$ ) of the source:

$$LE = \sqrt{\hat{\mathbf{r}} - \mathbf{r}} = \sqrt{(\hat{r}_x - r_x)^2 + (\hat{r}_y - r_y)^2 + (\hat{r}_z - r_z)^2} \quad (20)$$

e.g., for source-space ICA  $\hat{\mathbf{r}} = \mathbf{r}_{max}$ .

The error in estimated orientation of the desired dipole via source-space ICA is given by the orientation error (OE):

$$OE = \arccos \frac{\mathbf{q}^T(\mathbf{r}_{max}) \cdot \mathbf{q}(\mathbf{r})}{\|\mathbf{q}(\mathbf{r}_{max})\| \|\mathbf{q}(\mathbf{r})\|} \quad (21)$$

Source imaging via beamforming estimates the power of the source-space for a given epoch of EEG, resulting in a single tomographic map showing the power of the different brain regions for that epoch. Hence, a source can be localized if the power in the location of that source is stronger than the other background activity or other sources. The location of the sources can be determined by thresholding – i.e., if the power of certain regions becomes higher than a specified proportion of the maximum power, they can be considered as active sources in the EEG epoch due to an event in that epoch. As sensor-space ICA and source-space ICA produce independent components (ICs), visual inspection of ICs is needed to identify sources of interest.

#### Weak and strong sources

To evaluate performance on weak and strong sources, a single 10 Hz sinusoidal source was simulated with a weak (SNR = 0.2) and a strong (SNR = 2.0) magnitude, with orientation and location kept constant.

#### Discrimination of two closely-placed sources

Two sinusoidal sources of 10 and 12 Hz were placed bilaterally (symmetrical from the midline) for the case of shallow locations at  $z = 44$  mm and  $y = -18$  mm, and for the case of deep locations at  $z = 0$  mm and  $y = -18$  mm. The aim was to identify the minimum distance in the x direction between two sources that was required by source-space ICA to discriminate the two sources. Therefore, with keeping y and z constant, different x were used in this part to identify the minimum x for which the source-space ICA could separate the bilateral sources.

Since the head model was not spherical,  $\mathbf{r} = [0, 0, 0]$  mm was not the center of the brain and, in this study the center was assumed  $\mathbf{r} =$

$[0, -18, 0]$  mm. Therefore, sources placed closer to  $\mathbf{r} = [0, -18, 0]$  mm were considered deeper.

#### Cluster sources

Two clusters of sources were simulated with the size of each cluster being  $3 \times 3 \times 3$  voxels (i.e., 27 sources). The time-courses of the sources in each cluster were 5 Hz and 10 Hz sinusoids, and of 5 s to 8 s and 6 s to 9 s respectively. The centers of the clusters were  $[-6, -70, 4]$  mm and  $[-16, 0, 4]$  mm.

#### Multiple sources

To evaluate the ability of the algorithms to localize multiple sources, 10 sources were simulated with frequencies arbitrarily chosen from 2 to 20 Hz and SNRs from 0.2 to 1 and arbitrary orientations. The time-courses of the sources were fixed or damped sinusoids of 2 to 4 s duration, with an arbitrary start (from 0 to 8 s) on a 12 s background EEG. The simulated sources were scattered on two slices ( $z = -4$  mm and  $z = 36$  mm on MNI coordinates) with each slice having 5 sources (see Table 1 and Fig. 6).

#### Real EEG

To demonstrate and compare the application of the source-space ICA for localization and time-course reconstruction of real EEG sources, EEG data from 128 scalp sensors, using an ActiveTwo system, were downloaded from the SPM website (<http://www.fil.ion.ucl.ac.uk/spm/data/mmfaces>). These EEG data comprise 172 VEPs from 86 face and 86 scrambled face VEPs. Only the 86 VEPs for the faces were used in the current study. From these, 48 artifact-free VEPs were visually chosen, concatenated, and given to source-space ICA. The covariance matrix for the beamformer was measured over the 48 concatenated VEPs ( $48 \times 800$  ms) in line with other literatures (Cheyne et al., 2006; Fatima et al., 2013; Quraan and Cheyne, 2010; Robinson, 2004).

To identify the components of sensor- and source-space ICA with activity associated with the VEPs, the components were averaged over 48 trials to obtain single-trial components and then rectified. A Pearson correlation test was then applied between the components and a reference signal, to identify components with higher magnitudes during the 0–300 ms post-stimulus. The reference signal was a rectangular pulse of magnitude 1 from 0 to 300 ms and zero otherwise over the interval –200 to 600 ms (i.e., the same as for the VEP epoch). Components correlated with the reference signal were interpreted as sources due to the visual stimulus.

Evaluation of the beamformer approach was similar to source-space ICA in that the 48 VEPs were given to the beamformer and the power of the source-space was measured during 0–300 ms post-stimulus. For thresholding and source identification via beamforming, the power map of the source-space was thresholded at 80% of the maximum power, i.e., if the power of a voxel was higher than 80% of the maximum power in the source-space, it was considered a source and its location and time-course were shown.

#### Beamforming + ICA vs. ICA + beamforming

Although we are comparing the application of beamforming followed by ICA (source-space ICA) with sensor-space ICA followed by dipole fitting, it may seem that a better comparison could have been between source-space ICA and sensor-space ICA followed by a minimum-norm or a minimum-variance beamforming. However, sensor-space ICA followed by minimum-variance beamforming is less than ideal as the minimum-variance beamformer requires a covariance matrix of the sensor signals. If the only activity on the sensors becomes confined to a single independent component separated from other components by sensor-space ICA, the rank of the sensor covariance matrix will be 1,

**Table 1**

Specification of the 10 sources and summary of results for localization errors and SNR of reconstructed sources. LE: localization error, OE: orientation error, SNR; signal-to-ratio.

Source frequency and SNR	Location and orientation of source	Localization error, orientation error, and SNR via source-space ICA	Localization error and SNR via sensor-space ICA and dipole fitting	Localization error and SNR via beamformer
$s_1(t)$ $F = 2$ Hz SNR = 0.4	$\mathbf{r}_1 = [34, 40, -4]$ mm $\mathbf{q}_1 = [0.00, 0.70, 0.70]$	$\bar{\mathbf{r}}_1 = [34, 40, -14]$ mm LE = 10 mm, OE = 33° SNR = 2.7	$\hat{\mathbf{r}}_1 = [34, 50, -4]$ mm LE = 10 mm SNR = 2.2	Not found
$s_2(t)$ $F = 15$ Hz SNR = 0.3	$\mathbf{r}_2 = [4, 10, -4]$ mm $\mathbf{q}_2 = [0.00, 0.00, 1.00]$	$\bar{\mathbf{r}}_2 = [-36, 20, -24]$ mm LE = 46 mm, OE = 68° SNR = 2.1	$\hat{\mathbf{r}}_2 = [-36, 20, -4]$ mm LE = 41 mm SNR = 1.2	Not found
$s_3(t)$ $F = 6$ Hz SNR = 0.3	$\mathbf{r}_3 = [-36, -30, -4]$ mm $\mathbf{q}_3 = [1.00, 0.00, 0.00]$	$\bar{\mathbf{r}}_3 = [-46, -20, -4]$ mm LE = 14 mm, OE = 34° SNR = 1.7	$\hat{\mathbf{r}}_3 = [-46, -20, -4]$ mm LE = 14 mm SNR = 1.5	Not found
$s_4(t)$ $F = 8$ Hz SNR = 0.5	$\mathbf{r}_4 = [-26, -50, -4]$ mm $\mathbf{q}_4 = [0.00, 1.00, 0.00]$	$\bar{\mathbf{r}}_4 = [-26, -50, -4]$ mm LE = 0 mm, OE = 7° SNR = 2.0	$\hat{\mathbf{r}}_4 = [-36, -70, 6]$ mm LE = 24 mm SNR = 1.9	Not found
$s_5(t)$ $F = 10$ Hz SNR = 0.5	$\mathbf{r}_5 = [34, -70, -4]$ mm $\mathbf{q}_5 = [0.70, 0.70, 0.00]$	$\bar{\mathbf{r}}_5 = [34, -70, -4]$ mm LE = 0 mm, OE = 3° SNR = 1.9	$\hat{\mathbf{r}}_5 = [54, -70, 6]$ mm LE = 22 mm SNR = 1.9	$\hat{\mathbf{r}}_5 = [34, -60, -4]$ mm LE = 10 mm SNR = 0.6
$s_6(t)$ $F = 10$ Hz SNR = 0.7	$\mathbf{r}_6 = [-6, 30, 36]$ mm $\mathbf{q}_6 = [0.44, 0.18, 0.88]$	$\bar{\mathbf{r}}_6 = [-6, 30, 36]$ mm LE = 0 mm, OE = 1° SNR = 0.8	Not found	$\hat{\mathbf{r}}_6 = [-6, 30, 36]$ mm LE = 0 mm SNR = 4.0
$s_7(t)$ $F = 15$ Hz SNR = 0.3	$\mathbf{r}_7 = [44, 10, 36]$ mm $\mathbf{q}_7 = [0.45, 0.90, 0.00]$	$\bar{\mathbf{r}}_7 = [44, 10, 36]$ mm LE = 0 mm, OE = 3° SNR = 5.6	$\hat{\mathbf{r}}_7 = [54, 20, 36]$ mm LE = 14 mm SNR = 8.2	$\hat{\mathbf{r}}_7 = [44, 10, 36]$ mm LE = 0 mm SNR = 3.5
$s_8(t)$ $F = 8$ Hz SNR = 0.8	$\mathbf{r}_8 = [-26, -30, 36]$ mm $\mathbf{q}_8 = [0.00, 0.70, 0.70]$	$\bar{\mathbf{r}}_8 = [-26, -30, 36]$ mm LE = 0 mm, OE = 3° SNR = 0.9	$\hat{\mathbf{r}}_8 = [-36, -10, 46]$ mm LE = 24 mm SNR = 0.9	$\hat{\mathbf{r}}_8 = [-26, -30, 36]$ mm LE = 0 mm SNR = 3.7
$s_9(t)$ $F = 18$ Hz SNR = 0.4	$\mathbf{r}_9 = [4, -60, 36]$ mm $\mathbf{q}_9 = [0.00, 1.00, 0.00]$	$\bar{\mathbf{r}}_9 = [4, -70, 36]$ mm LE = 10 mm, OE = 0° SNR = 10.6	$\hat{\mathbf{r}}_9 = [34, -60, 36]$ mm LE = 30 mm SNR = 9.1	$\hat{\mathbf{r}}_9 = [4, -70, 36]$ mm LE = 10 mm SNR = 3.9
$s_{10}(t)$ $F = 20$ Hz SNR = 0.2	$\mathbf{r}_{10} = [24, -70, 36]$ mm $\mathbf{q}_{10} = [0.57, -0.57, 0.57]$	$\bar{\mathbf{r}}_{10} = [24, -70, 36]$ mm LE = 0 mm, OE = 23° SNR = 5.2	$\hat{\mathbf{r}}_{10} = [24, -70, 36]$ mm LE = 0 mm SNR = 2.7	Not found

the matrix will not be invertible, and, therefore, regularization of the covariance matrix is necessary. A low-rank covariance matrix, together with regularization of the inverse matrix, degrades the spatial resolution of a minimum-variance beamformer and it will act like a minimum-norm filter. This may be why Ventouras et al. (2010) applied sLORETA rather than a minimum-variance beamformer for sensor-space independent components, despite other studies (e.g., Sekihara and Nagarajan, 2008) showing the superior spatial resolution of the minimum-variance spatial filters over their minimum-norm counterparts. In contrast, in source-space ICA, the beamformer is applied first on the sensor data and, therefore, the rank of the covariance matrix will be the same or close to the number of the sensors (also depending on the length of the data). We undertook a brief comparison to see how the order of application of ICA and beamforming affects source separation and spatial resolution. In this comparison, we compared source-space ICA (WNMV beamforming + ICA) to sensor-space ICA followed by the WNMV beamformer (ICA + WNMV). We also made the same comparison for the weight-normalized minimum-norm (WNMN) beamformer (Dale et al., 2000). The simulated EEG for these comparisons was the 10 simulated sources described in the Multiple sources section. In the case of sensor-space ICA, data with rank 1 was made by removing other independent components and leaving only the components of interest. The WNMV beamformer or the WNMN filter was applied to this rank 1 data to project the sensor data into the source-space.

In a further quantitative comparison, 2160 simulations were run for each of the three techniques: (1) WNMV beamformer, (2) WNMV + ICA, and (3) ICA + WNMN filter. These simulations comprised a source at different depths, magnitudes, and orientations. The depths were from [0 0 0] mm to [0, -90, 0] mm (moving in the y direction every 10 mm), the orientations were from [1, 0, 0] to [-1, 0, 0] (corresponding to 180 deg rotation around the z vector in 8 samples), and the SNRs of the simulated source were 0.01, 0.10, 0.25, 0.50, 0.80, 1.20, 2.20, and 2.75. The simulations were applied to the EEG backgrounds from 3 subjects. Therefore, there were 10 (depths) × 8 (orientations) × 9

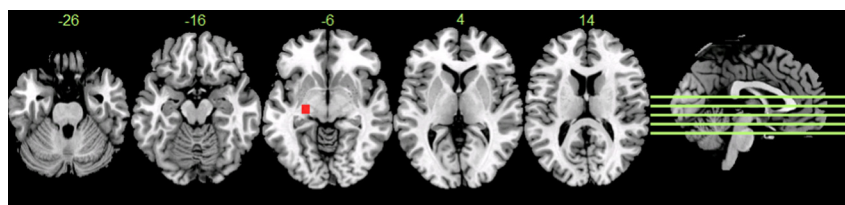
(magnitudes) × 3 (EEG backgrounds) = 2160 simulations per technique. The length of the simulated EEG was 10 s and the simulated source was a 10 Hz sinusoid from 6 to 9 s and zero otherwise. In the case of the beamformer, for every simulation, the beamformer was run to produce the source-space data and the power at each voxel was then estimated via neural activity index for the 6–9 s period, and the voxel with the maximum power was considered as the source. The time-course of the identified source was the neural activity index at each time sample for that voxel and its SNR could be estimated. In the case of source-space ICA and sensor-space ICA, source identification was done via Pearson's correlation between the absolute value of the independent time-courses and a reference signal. The *i*th independent time-course with the highest correlation coefficient was considered to be the source of interest, and in the case of source-space ICA, the voxel with the greatest value in the *i*th column of  $\mathbf{G}$  (in fact  $\bar{\mathbf{g}}_i$  which contains the norm of  $\mathbf{g}_i$  in x, y, and z directions) was considered to be the location of the source. In the case of the sensor-space ICA, the same correlation test was applied and the WNMN filter was applied to the *i*th topographic map (mixing vector) to project it to the voxels and the voxel with the greatest value was considered as the location of the source and the localization error was the distance between this location and the actual location of the simulated source. The reference signal had the same length as the independent components (10 s) and was '1' from 6 to 9 s and '0' otherwise.

**Results**

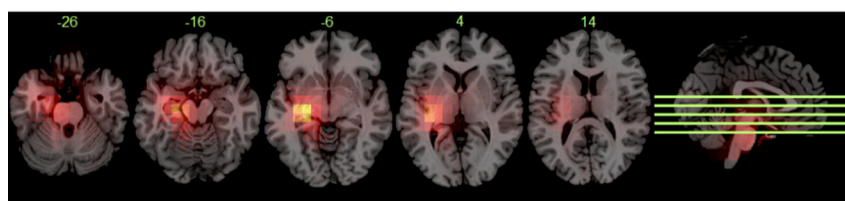
The actual locations of the sources are shown as the first sub-figure, called *ground truth*, in Figs. 3–6.

*Weak and strong sources*

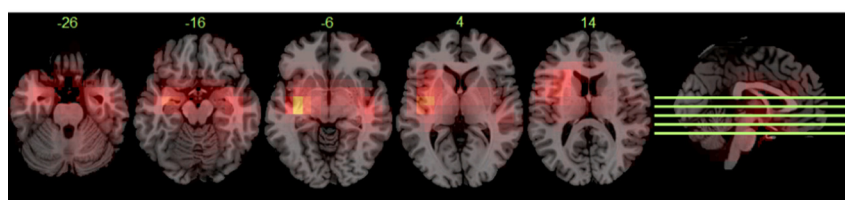
With an SNR of 2, all three algorithms were able to localize the source of interest (Figs. 3b, c, d). The LE for sensor-space ICA/dipole



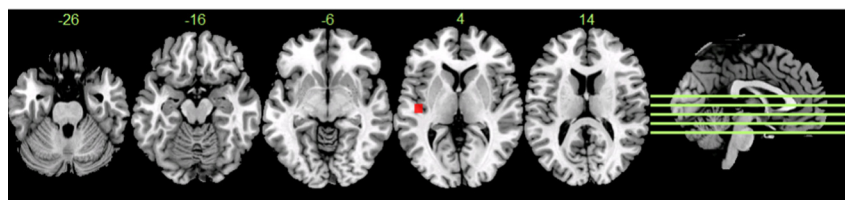
(a) Ground truth



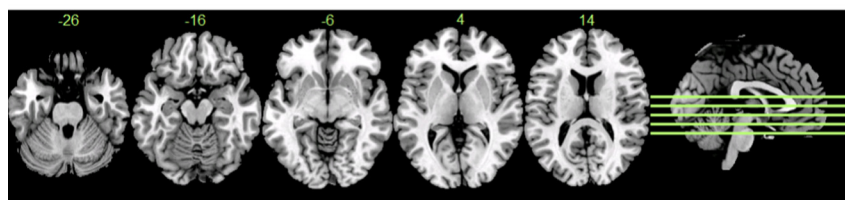
(b) Source-space ICA, SNR = 2.0



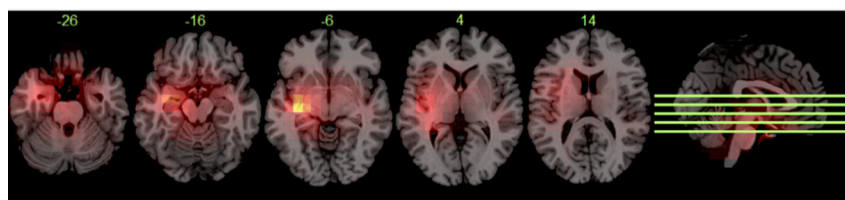
(c) Source-space ICA, SNR = 0.2



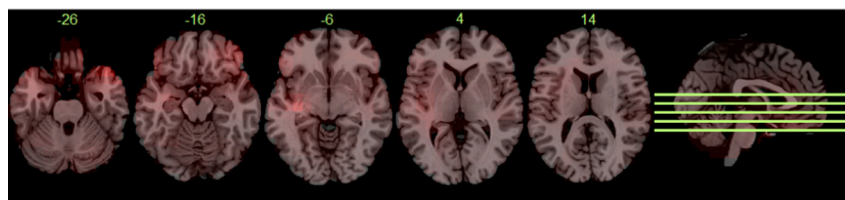
(d) Sensor-space ICA/dipole fitting, SNR = 2.0



(e) Sensor-space ICA/dipole fitting, SNR = 0.2



(f) Beamformer, SNR = 2.0



(g) Beamformer, SNR = 0.2

**Fig. 3.** Localization of a strong source, SNR = 2.0, and a weak source, SNR = 0.2, via source-space ICA, sensor-space ICA/dipole fitting, and WNMV beamformer. Sensor-space ICA failed to separate the weak source of interest as an independent component (e).

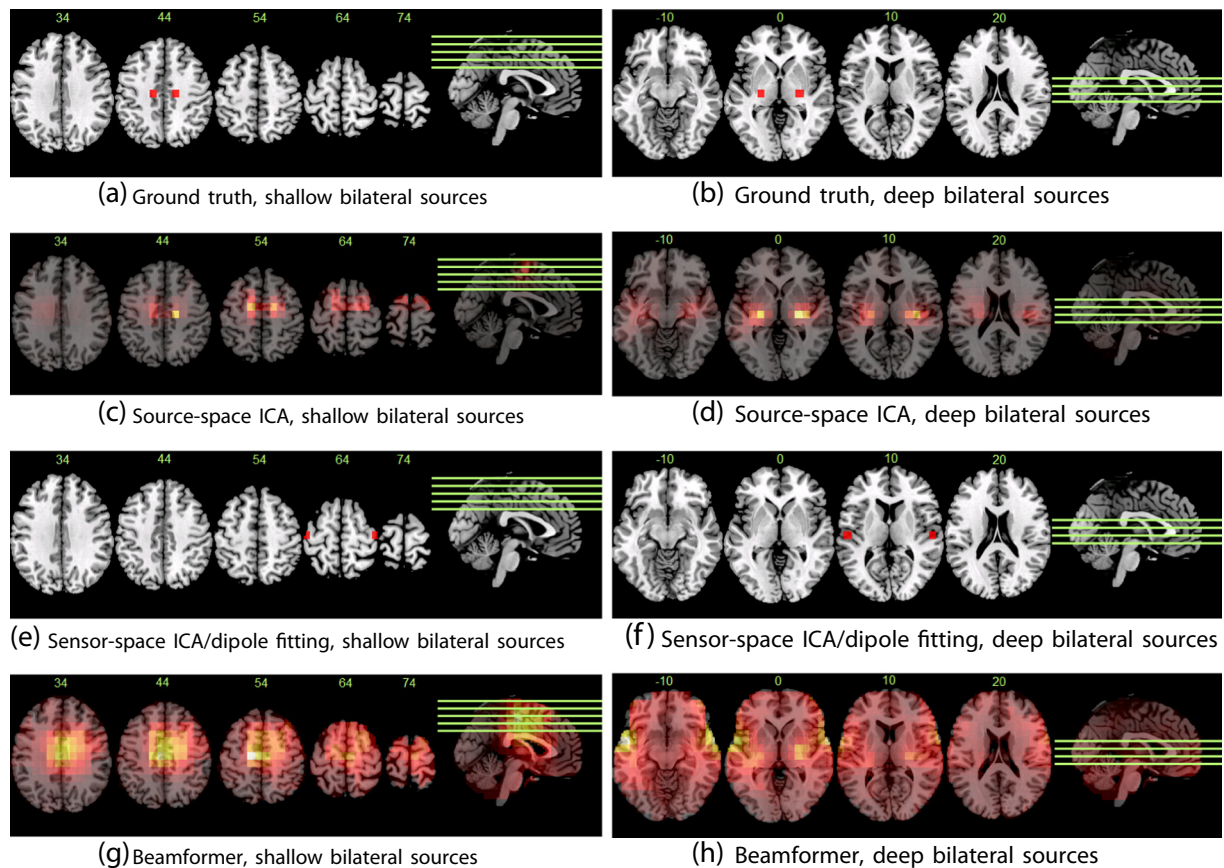


**Fig. 4.** Localization of shallow ( $y = -18$  mm and  $z = 44$  mm) bilateral sources and deep ( $y = -18$  mm and  $z = 0$  mm) bilateral sources via source-space ICA, sensor-space ICA/dipole fitting, and WNMV beamformer. Minimum inter-source distances of 26 mm and 42 mm were needed for source-space ICA to separate the shallow and deep bilateral sources respectively.

fitting was 20 mm, whereas source-space ICA had 0 mm LE and the WNMV beamformer was 10 mm. With  $\text{SNR} = 0.2$ , sensor-space ICA failed to identify the source of interest (Fig. 3e). Source-space ICA identified the source of interest with 10 mm LE (Fig. 3c), and the power map via the beamformer shows a very weak source with 10 mm LE (Fig. 3f). However, in the map provided by the beamformer (Fig. 3f), although the source of interest is visible, it is not the dominant source as there are other stronger background activities with their voxels having higher powers. This is due to the fact that plotting the power measured by a beamformer will show only the stronger sources and, therefore, if the source of interest is weak, it may not be distinguishable from other background activities. In the maps provided by source-space ICA, the source of interest was the dominant source as it was separated from other background activities.

#### Discrimination of two closely-placed sources

After repeated examination of the bilateral sources at different separations in the x direction (i.e., y and z kept constant) it was found that when the bilateral sources were shallow ( $y = -18$  mm and  $z = 44$  mm), the minimum distance that source-space ICA needed to separate the two sources was 26 mm (Fig. 4c), compared to 42 mm when the sources were deep ( $y = -18$  mm and  $z = 0$  mm) (Fig. 4d). The LE was 0 mm. Although source-space ICA was able to separate the two sources spatially (as shown in Figs. 4c, d), it failed to separate the time-courses of these two sources and identified time-courses of a mixture of 10 and 12 Hz. Sensor-space ICA also failed to separate the time-courses of two sources, and dipole fitting (with a bilateral constraint) had a 30-mm LE for both deep and shallow sources (Figs. 4e, f). For the shallow sources, the power map via the beamformer shows the middle of the two sources with highest intensity (sources were merged)

(Fig. 4g). However, for the deep (and greater spaced) sources, the power map shows a weak bilateral source (Fig. 4h).

#### Cluster sources

Source-space ICA identified two clusters, with the center of the posterior cluster having a 0-mm LE and the center of the anterior cluster having a 10-mm LE (Figs. 5b, c). Sensor-space ICA identified two sources, with the distance of these two from the center of the clusters being 10 mm LE for the posterior source and 20 mm for the anterior cluster (Fig. 5d). The beamformer identified two sources (Fig. 5e) but the posterior source is more similar to a single source than a cluster source. The center of the posterior source has a 0-mm LE and the center of the anterior cluster has a 10-mm LE.

#### Multiple sources

Of the 10 simulated sources, source-space ICA identified 10 sources (Fig. 6b), sensor-space ICA identified 9 sources (Fig. 6c), and the WNMV beamformer identified 5 sources (Fig. 6d) (Table 1). As mentioned earlier, source-space ICA provides a tomographic map for every identified source. However, to avoid having 10 tomographic maps, we only show one map with the voxel with the highest intensity for every identified component by source-space ICA. As for the power map via the beamformer, only the voxels with higher intensities than the background activity are shown. From 10 sources identified by source-space ICA, 6 sources had an LE of 0 mm, 3 had LEs between 10 and 20 mm, and one had an LE of 46 mm. From 9 sources identified by sensor-space ICA, 1 source had an LE of 0 mm, 3 had LEs between 10 and 20 mm, and 5 had LEs between 20 and 42 mm. In the power map via the beamformer, 5 of the sources had lower power than the

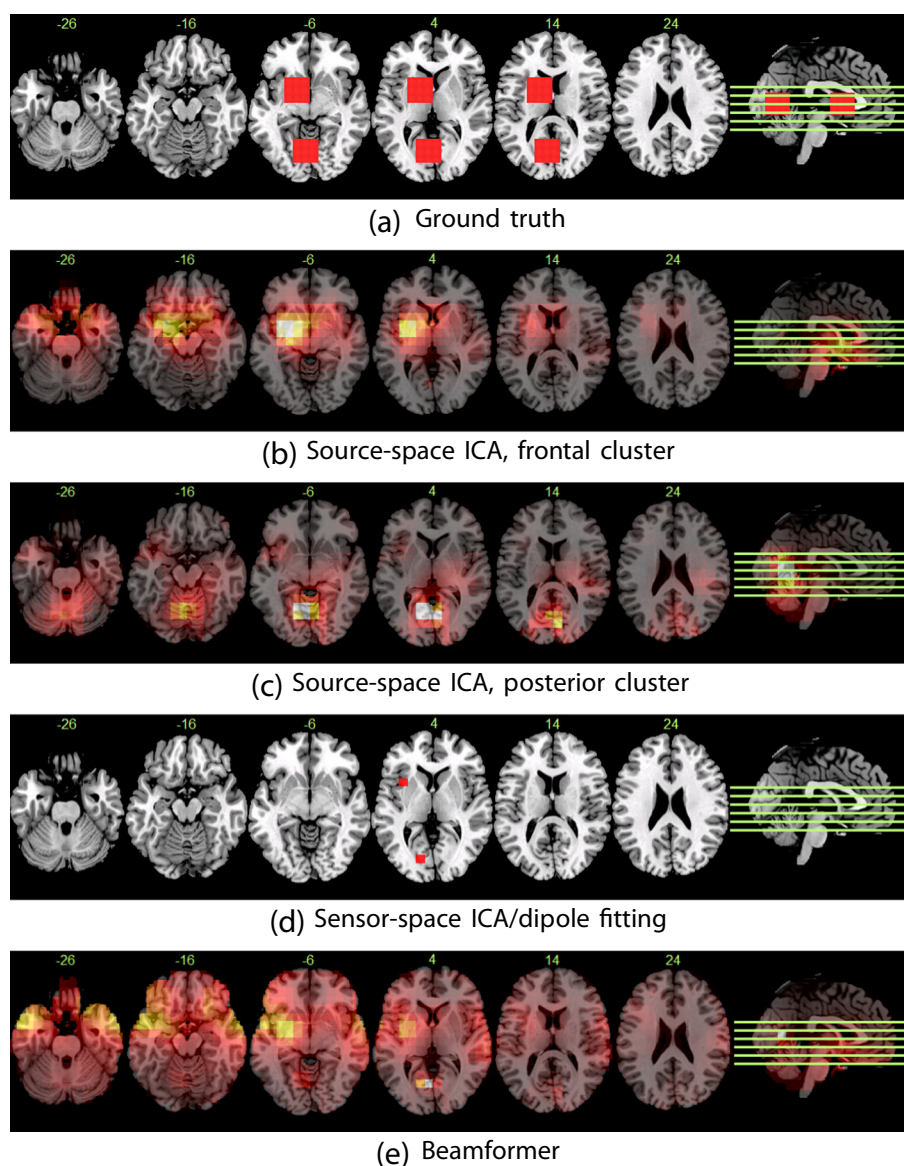


**Fig. 5.** Localization of two clusters of sources, via source-space ICA, sensor-space ICA/dipole fitting, and the WNMV beamformer. As source-space ICA provides a tomographic map for each of the two components, the maps of each component are shown separately, (b) and (c). Sensor-space ICA/dipole fitting also provides a separate location for each component, however, for simplicity they are superimposed on each other (d). The power map via the beamformer is obtained over the period in which two clusters were active (e).

background activity and, therefore, are not visible in the map. From the 5 sources identified by the beamformer, 3 had LEs of 0 LE and 2 had LEs of 10 mm. The time-course of the 10 sources (ground truth) and the reconstructed time-courses via the three approaches are shown in Fig. 7.

For the beamformer and power measurement of the source-space, first the power of the source-space was measured over the 1–10 s epoch covering the activation of all of the sources. However, only two sources (6 and 8) had higher power than the background activity (Fig. 8f). To be able to detect more sources via the beamformer, the power measurement was applied individually for 10 epochs when each of the 10 sources was active. In such a way it was possible to detect 5 sources. Both sensor-space ICA and source-space ICA were unable to separate the time-courses of sources 6 and 8 since the two sources had similar frequencies (10 and 8 Hz), were active at almost the same time (6.0–9.0 s and 6.5–9.5 s) and were spatially close to each other, making it difficult for ICA to separate the time-courses (Figs. 7y and z and also Figs. 8b and d). The application of dipole fitting to the sensor-space ICA component found a location between sources 6 and 8 (Fig. 6c at  $z = 46$ ), whereas source-space ICA spatially separated the two sources with 0 localization error (Fig. 6b at  $z = 36$ ; also Fig. 8c).

As the ability to estimate the orientation of sources (Eq. (19)) is an important feature of source-space ICA, the estimated source orientations for the 10 sources are shown in Table 1. More details on the 10-source simulation are given in Supplementary Figs. 1–5.

#### Real EEG with VEPs

The average VEPs for the 128 channels are shown in Fig. 9. However, the non-average VEPs were given to the source-space ICA. Source-space ICA was set to identify 83 components as the rank of signal matrix  $\mathbf{S}$  was 83. The result of correlation test between the sensor- and source-space ICA components and the reference signal (Fig. 10a) shows 6 components of source-space ICA with correlation coefficients,  $r$ , higher than 0.1, of which 5 components ( $IC_9$ ,  $IC_{13}$ ,  $IC_{27}$ ,  $IC_{31}$ , and  $IC_{63}$ ) have  $r > 0.3$  and one ( $IC_{41}$ ) has  $r = 0.24$ . Fig. 10 shows which components are time locked to the stimulus. Time-courses of these components and their corresponding tomographic maps are shown in Fig. 11. As ICA cannot retain the polarity of the sources, the time-courses are adjusted in such a way that all of the ICs have their peaks in the positive direction.

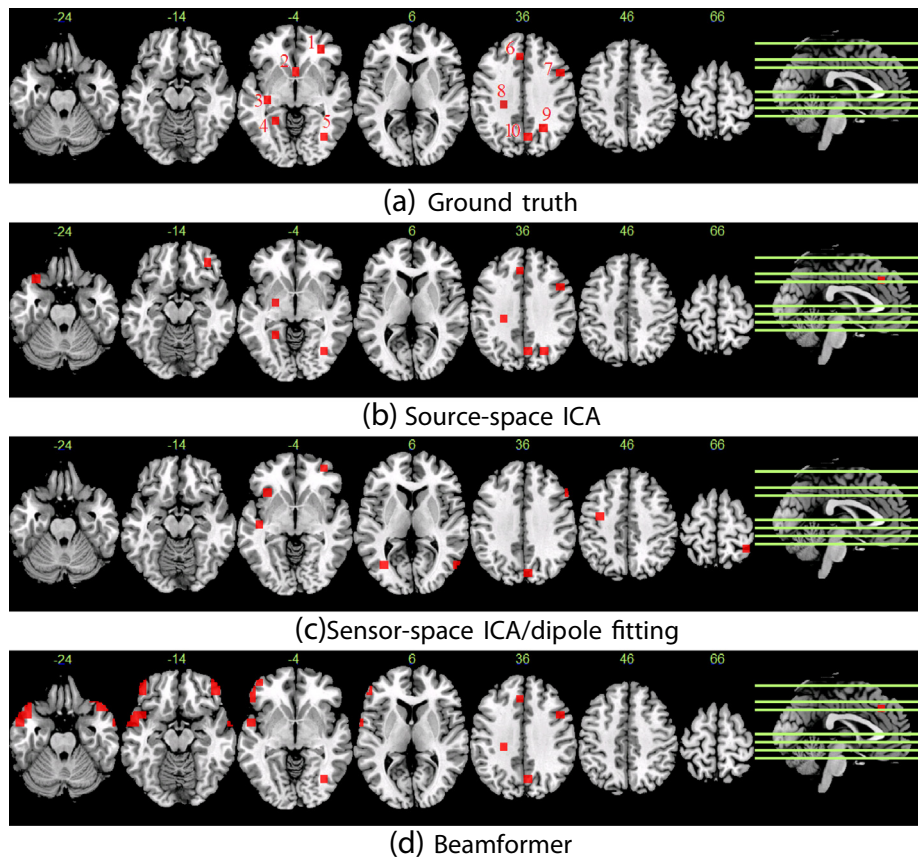


**Fig. 6.** Localization of 10 sources placed on two axial slices ( $z = 36$  and  $z = -4$  mm). Details of the location, orientation, and SNR of the simulated sources (i.e., ground truth) are provided in Table 1.

The time-courses shown in Fig. 11 are averages of the 48 events for the ICs.

$IC_{13}$  has the earliest peak, 65 ms, and has activations in the right occipital cortex area and posterior inferior temporal sulcus/gyrus.  $IC_{31}$  has a peak at 100 ms and it shows focal activation on the left occipital cortex.  $IC_{63}$  has a peak at 130 ms and is located in the right calcarine fissure.  $IC_{27}$  has a peak at 155 ms and shows activation mostly in the right precuneus cortex and partially in the left lateral occipital cortex and posterior fusiform gyrus.  $IC_9$  has a peak at 180 ms and shows activations in the precuneus cortex, superior frontal gyrus, and left calcarine fissure.  $IC_{41}$  has a peak at 230 ms and a second peak at 325 ms and shows activity focally in the precuneus cortex.

The correlation coefficients for components of the sensor-space ICA (Fig. 10b) show 3 components ( $IC_1$ ,  $IC_6$ , and  $IC_{64}$ ) with  $r > 0.2$ . Dipole fitting of these components is shown in Fig. 12.  $IC_6$  has peaks at 65 ms and 100 ms and is similar to a mixture of  $IC_{13}$  and  $IC_{31}$  from source-space ICA. Dipole fitting of  $IC_6$  (Fig. 12a) shows a central area in the brain as the origin of this component.  $IC_{64}$  has a peak at 130 ms and is similar to  $IC_{63}$  from source-space ICA but has two smaller peaks at 100 and 200 ms, whereas  $IC_{63}$  of source-space ICA has only one peak. Dipole fitting of  $IC_{64}$  (Fig. 12c) shows that the origin of the component is located in the right side of the occipital cortex.  $IC_1$  has its highest peak at 160 ms and is similar to a mixture of  $IC_{27}$ ,  $IC_{63}$  and  $IC_{41}$  of source-space ICA since the  $IC_1$  of sensor-space ICA has two other smaller peaks at 130 and 240 ms. Dipole fitting of  $IC_1$  (Fig. 12e) shows that the origin of the component is located in the left precuneus cortex.

Source imaging via beamforming and power measurement of the source-space is shown in Fig. 13. Fig. 13a shows the power of the source-space without thresholding and Fig. 13b shows the same map after 80% thresholding. As frontal ocular artifact is much stronger than the VEP-related brain area, it will be the only area to pass the threshold.

To improve the result of power mapping via beamformer, we first removed the ocular-related components of the EEG by visual inspection of the ICA components, and then performed the power measurement of the source-space again. In the second step, the power of the prior  $-200$ – $0$  ms was subtracted from the power of the  $0$ – $300$  ms of the source-space. This step reduces the baseline power of the source-space and helps identify sources related to the VEPs. The power of the source-space was then thresholded at 80% (Fig. 14a). Three clusters of voxels passed the threshold, located bilaterally in the calcarine fissure (sources 1 and 2) and one in the right posterior inferior temporal gyrus (source 3). These areas are similar to  $IC_{13}$ ,  $IC_{31}$ , and  $IC_{63}$  for source-space ICA. Source 1 in the right calcarine fissure has 3 magnitude peaks at 65 ms, 130 ms, and 150 ms (Fig. 14b). The last two peaks merged as a single they occurred close to each other. Source 2 in the left calcarine fissure also has 3 peaks at 100 ms, 150 ms, and 190 ms (Fig. 14c). Source 3 in the right posterior inferior temporal gyrus has 1 peak at 65 ms and smaller peaks at 180 ms and 250 ms (Fig. 14d).

#### Beamforming + ICA vs. ICA + beamforming

Comparisons between WNMV/WNMN + ICA and ICA + WNMV/WNMN are provided in Supplementary Figs. 1–5. Based on these comparisons, the separation power of ICA is similar for all four combinations. However, in terms of spatial resolution, WNMV + ICA (WNMV-based source-space ICA) is superior to WNMN-based source-space ICA and sensor-space ICA + WNMV/WNMN. WNMV-based source-space ICA provided sharp images for the location of the 10 sources, except source 2, whereas the other alternatives had blurry images (poor spatial resolution). The worst spatial resolution (i.e., highly blurry) was obtained from ICA + WNMN (as shown in Supplementary Fig. 5). We estimated the average spatial FWHM of these four combinations of the techniques

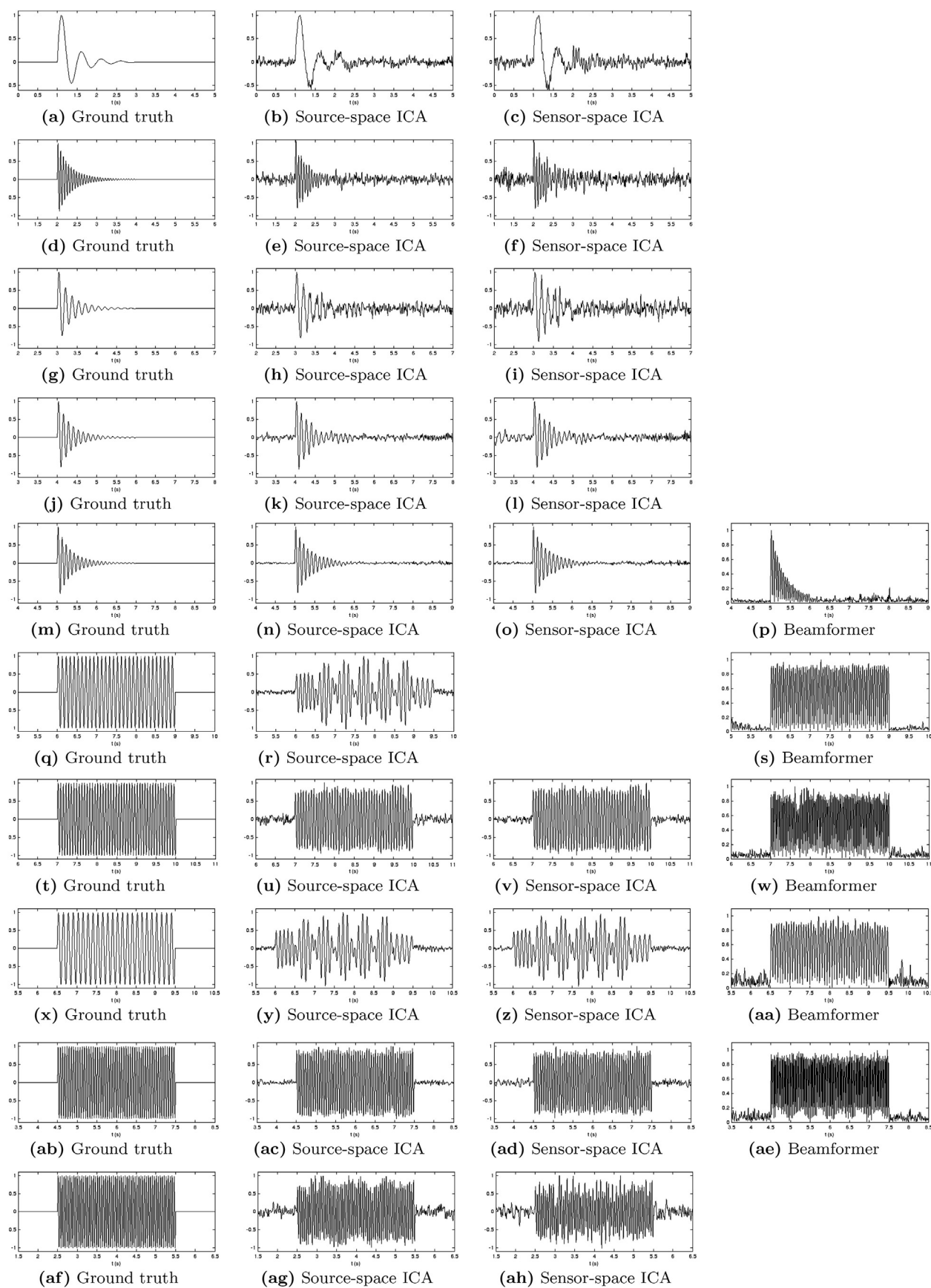


**Fig. 7.** Time-courses of the 10 simulated sources in a 10 s EEG epoch. The first column from the left shows the ground truth, the second column shows the time-courses of the components identified by source-space ICA, the third column shows the components identified by sensor-space ICA, and the fourth column shows the magnitude time-series of the sources identified by the beamformer. The SNR of these time-courses is shown in Table 1 and their localization in Fig. 6.

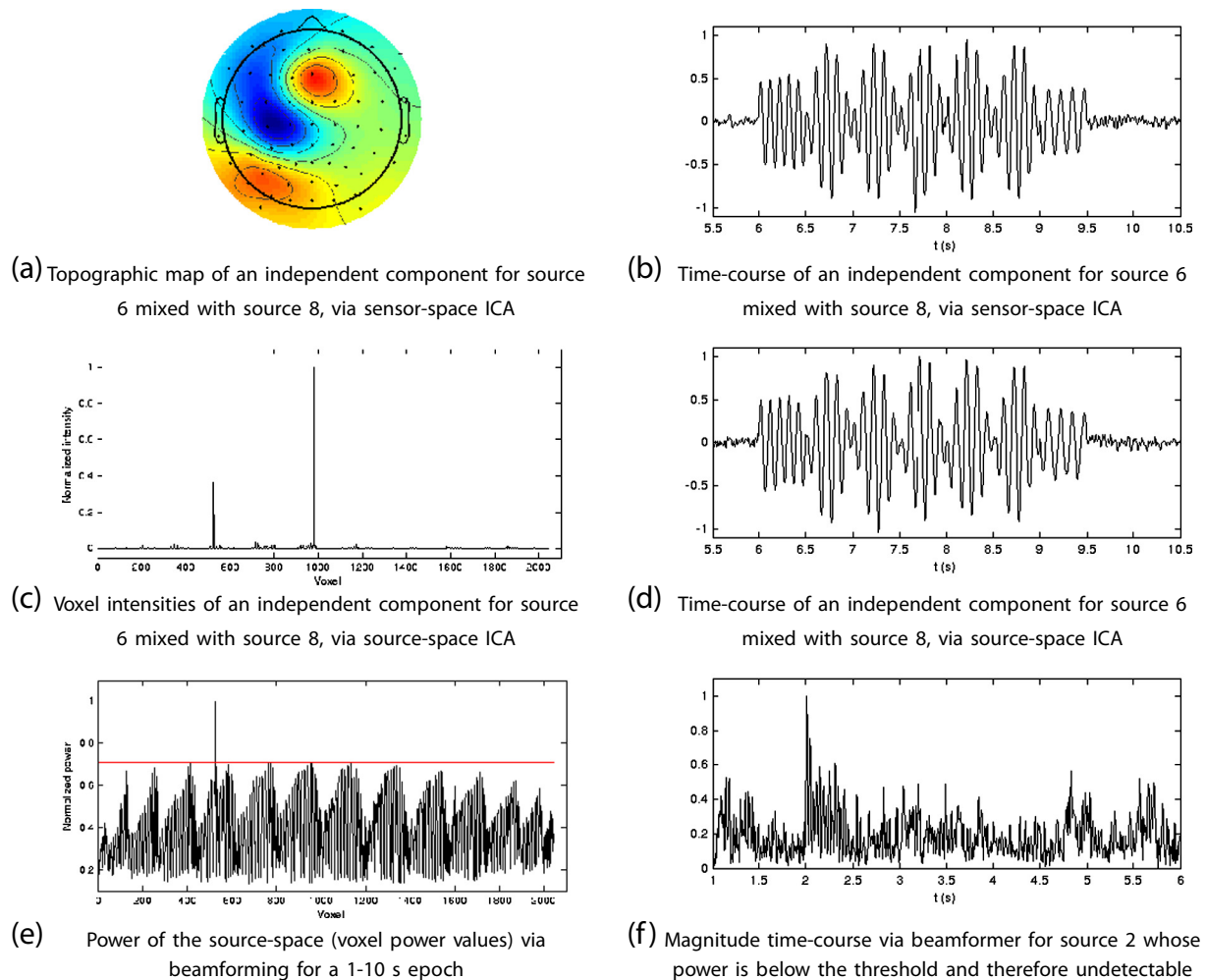


**Fig. 8.** An illustration of how both beamforming and sensor-space ICA failed to detect some of the sources in the multiple source analysis. Figure (a) is the topographic map for an independent component identified by sensor-space ICA and figure (b) is the time-course for this component. Similar to the topographic map, the time-course is a mixture of sources 6 and 8 and, therefore, dipole fitting for this component found a location somewhere between sources 6 and 8, as shown in Fig. 6c at  $z = 46$ . Figure (c) shows voxel intensities (Eq. (17)) for a component identified by source-space ICA. Source-space ICA also failed to separate the time-courses of sources 6 and 8 (figure (d)) but, the two sources are spatially separated with zero localization error (figure (c)). The two spikes in figure (c) are the intensities of voxels where sources 6 and 8 are located. Figure (e) shows the power of the source-space for a period of 1–10 s when all the 10 sources were active. The red line shows the threshold which separated the power of the sources from the power of the background activity, i.e., all voxels with power below the red line were removed from the tomographic maps, with only sources 6 and 8 having a higher power than the background activity during the 1–10 s of EEG epoch. Figure (f) is an example of the magnitude time-course of source 2, reconstructed by the beamformer, which had a lower power than the background activity and therefore did not pass the threshold. Figure (f) can be compared to the other two techniques and the ground truth in the second row of Fig. 7.

for 10 multiple sources: WNMV + ICA = 10 mm, ICA + WNMV = 45 mm, WNMN + ICA = 50 mm, and ICA + WNMN = 55 mm. These values may change with other factors (especially number of scalp sensors), but they provide an approximate estimation of the relative spatial resolution of these four combinations.

Fig. 15 shows the quantitative evaluation of three approaches (1) WNMV, (2) WNMV + ICA, and (3) ICA + WNMN, with respect to changes in the magnitude (SNR<sub>in</sub>), depth, and orientation of a simulated source. The localization error and SNR of the reconstructed source (SNR<sub>out</sub>) were the measures used in the evaluation. Based on Figs. 15a, c, and e, the ICA + WNMN has a generally higher source localization error than the other two approaches and is sensitive to changes in source orientation. All approaches had lower localization error for the stronger sources, but, based on Fig. 15b, unlike the other two approaches, ICA + WNMN had a higher localization error for cortical sources. Based on Fig. 15a, the localization error for ICA + WNMN will never reach zero, whereas the other two approaches will have a zero localization error (regardless of depth and orientation) for stronger sources (i.e., SNR<sub>in</sub> ≥ 1.2). The worst performance for the proposed WNMV + ICA approach was obtained with deep weak sources. In terms of the quality of the reconstructed source time-course, based on

Figs. 15b, d, and f, the two approaches incorporating ICA had similar performances and both had a higher SNR<sub>out</sub> to that of beamforming by itself, as in beamforming approach the neural activity index at each time sample (magnitude time-series) is used for time-course reconstruction, which can only be positive values.

## Discussion

In this paper, we have described and formulated source-space ICA as a novel technique for separation, localization, and time-course reconstruction of EEG sources. Source-space ICA is the application of minimum-variance beamforming followed by ICA. This combination of minimum-variance beamforming and ICA results in having the high spatial resolution of the beamformer, plus substantially improved identification and localization of multiple weak and strong sources, which are challenging for current source imaging techniques. In source-space ICA, source imaging is obtained via back-projection of the ICA mixing coefficients, as opposed to more popular methods based on back-projection of the power at each location (such as neural activity index).

As the orientations of sources are not known in EEG and MEG, vector beamforming is applied to reconstruct the time-courses of the sources

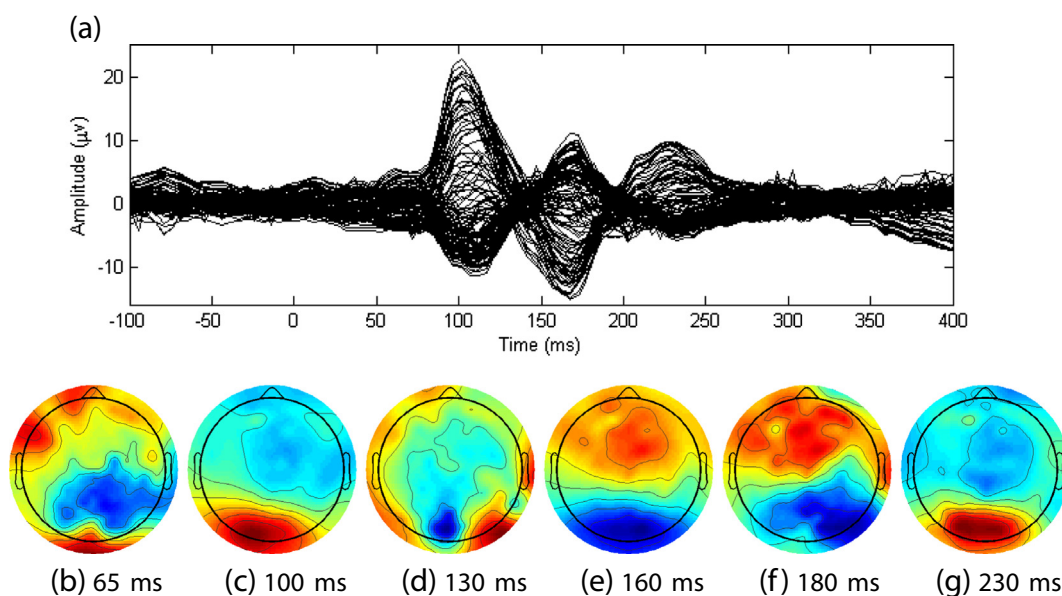


**Fig. 9.** (a) Average VEPs (faces) for the 128 channels. The average VEPs were obtained over 48 VEPs. Topographic maps of the VEPs at (b) 65 ms, (c) 100 ms, (d) 130 ms, (e) 160 ms, (f) 180 ms, and (g) 230 ms.

in 3 orthogonal directions. The usual approach to estimate activity in a given voxel is to merge the 3 orthogonal time-courses to get magnitude (i.e.,  $\hat{s}^2(t, \mathbf{r}_b) = \hat{s}_x^2(t, \mathbf{r}) + \hat{s}_y^2(t, \mathbf{r}) + \hat{s}_z^2(t, \mathbf{r})$  or neural activity index). However, this can only produce positive values and, hence, is not the time-course of sources. An alternative for reconstruction of a single time-course for each source is the scalar beamformers, which are themselves dependent on a prior good estimate of the source-orientation, via techniques such as grid search (Robinson and Vrba, 1998). Additionally, as shown by Jonmohamadi et al. (2014b) and Fig. 15, merging the time-courses via calculating the magnitude degrades the SNR of the reconstructed time-courses as all the samples become positive, e.g., in the case of  $\hat{s}^2(t, \mathbf{r}_b)$ , if the source of interest at ' $\mathbf{r}_b$ ' has a moment only in the x direction, the other two directions will only contribute noise power to  $\hat{s}^2(t, \mathbf{r}_b)$  and degrade the SNR of the  $\hat{s}^2(t, \mathbf{r}_b)$  (which is problematic for weak sources). In contrast, ICA identifies in which directions the maximum contributions of an independent component are and puts higher coefficients on those directions and minimizes the other directions. Therefore, source-space ICA acts as a scalar beamformer and gives a single time-course for each identified source, and estimates the orientation of the source as shown via Eq. (19). This means that source-space ICA is also a source-orientation estimation technique and is superior to the well-known grid search of Robinson and Vrba

(1998) which assumes that the source of interest is the strongest source in the source-space.

Source-space ICA is superior to source-space power mapping via beamforming for identification of multiple weak and strong sources. This is because source-space ICA can separate weak and strong sources and provide separate tomographic maps for each of the identified components, whereas the power map of the source-space via beamforming is unable to distinguish weaker sources in the presence of stronger sources. Source-space ICA is also able to localize sources with higher spatial accuracy than ICA plus dipole fitting/minimum-norm filter.

On reconstruction of VEP sources, source-space ICA was able to identify 6 sources time-locked to stimuli. The 4th and 5th ICs have latencies of 140–200 ms following the presentation of the stimulus and correspond to the N170. The localization of these ICs is in line with other studies of VEPs for EEG and MEG in the lateral occipital cortex/posterior fusiform gyrus (e.g., Rossion and Jacques (2012) and Owen et al. (2012)). Sensor-space ICA identified 3 components and all of these had 2 or 3 amplitude peaks. In contrast, the components identified by source-space ICA had only one large peak.

The simulation of 10 multiple sources (Multiple sources section) showed that source-space ICA had smaller localization error than

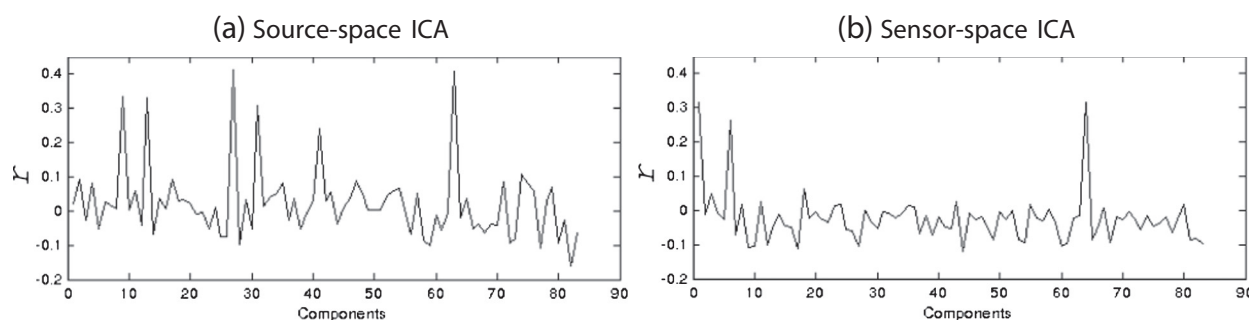


**Fig. 10.** The correlation coefficients  $r$  for (a) components of source-space ICA and (b) components of sensor-space ICA. A Pearson correlation test was applied between the components and a reference signal, to identify components with higher magnitudes during the 0–300 ms post-stimulus. The reference signal was a rectangular pulse of magnitude 1 from 0 to 300 ms and zero otherwise over the interval  $-200$  to 600 ms (i.e., the same as for the VEP epoch). Components correlated with the reference were interpreted as sources due to the visual stimulus.

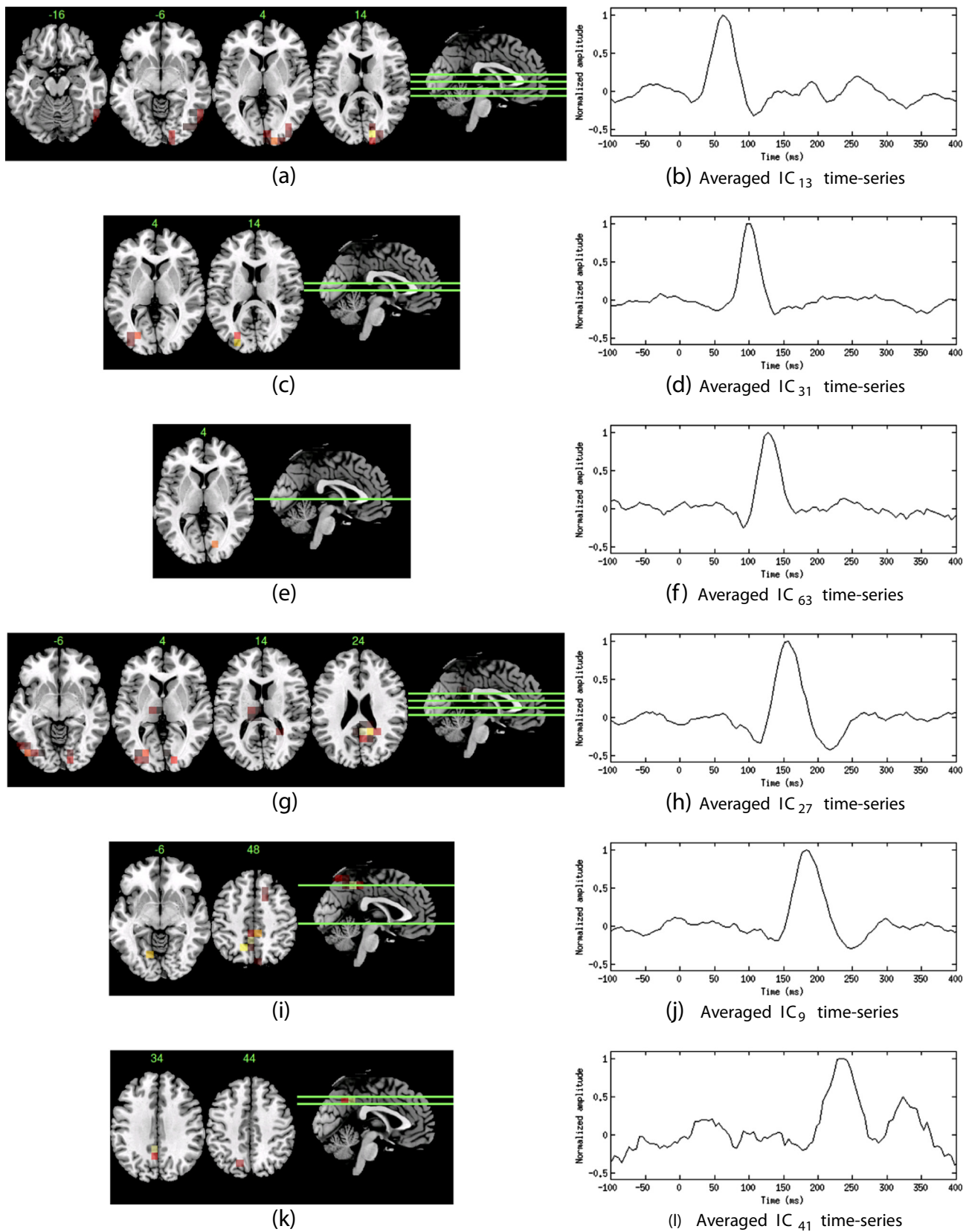


**Fig. 11.** Time-courses of the ICs identified via source-space ICA and time-locked to the VEPs, based on Fig. 10a. The left figures show the location of the ICs and the right figures show the averaged time-courses of the ICs.

sensor-space ICA followed by dipole fitting, albeit marginally (Wilcoxon:  $p = 0.062$ ), of the 9 sources identified by both sensor-space ICA and source-space ICA. Source-space ICA was also successful for the

localization and spatial separation of the independent components which are mixtures of more than one source (e.g., Fig. 8c). In contrast, the quality of the reconstructed time-course in terms of SNR was

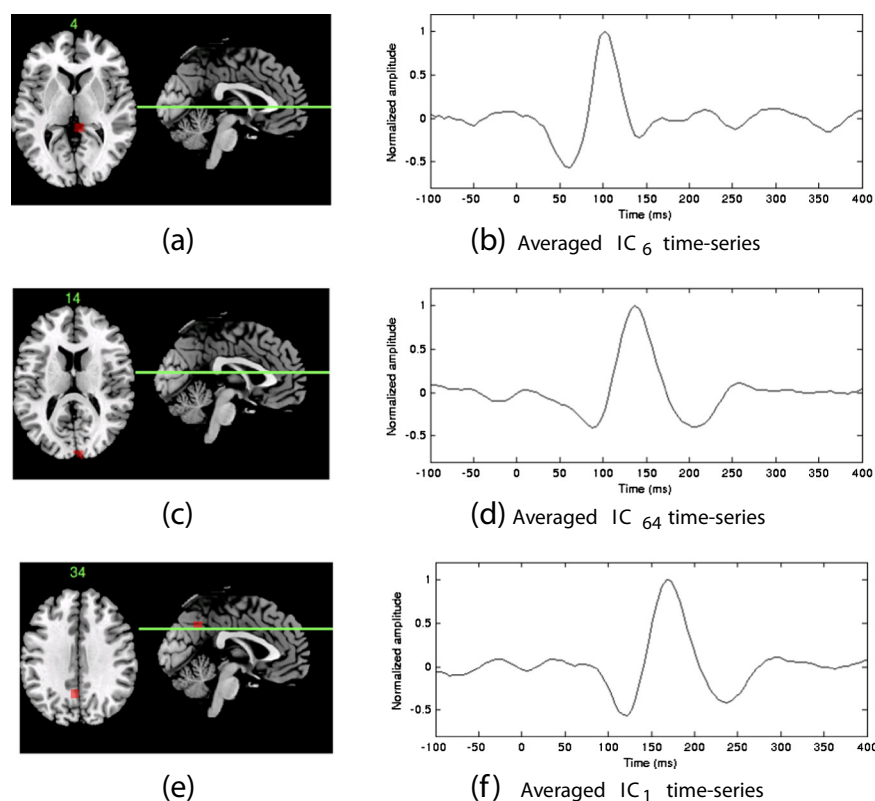


**Fig. 12.** Time-courses of the ICs identified via sensor-space ICA and time-locked to the VEPs, based on Fig. 10b. The left figures show the location of the ICs and the right figures show the averaged time-courses of the ICs.

essentially the same ( $p = 0.30$ ). Based on 2160 simulations per technique, source-space ICA had a significantly lower localization error than sensor-space ICA ( $p < 0.001$ ). There was no significant difference between localization error of source-space ICA and beamforming on its own ( $p = 0.076$ ).

The beamformer and power mapping approach has the similar spatial accuracy as the source-space ICA. However, if the sources of interest are weaker than background activity or other sources, they may not pass the power threshold and, therefore, not appear in the maps. An example of this situation is shown in Fig. 13 where the ocular artifacts

have much higher power than the VEP sources. It was only after artifact removal that the power plot was able to show the VEP sources (Fig. 14). Similar results regarding the effect of ocular artifacts on beamforming are shown in Fatima et al. (2013). Compared with the beamforming and power mapping approach, source-space ICA is far more robust to artifacts as it separates the activity of different brain sources and artifacts and provides a unique tomographic map for each. That is, the artifacts have their own maps and cannot interfere with the maps of other sources. For example, in Fig. 8c, except for the two voxels containing sources 6 and 8, the voxels have near zero intensities which provides

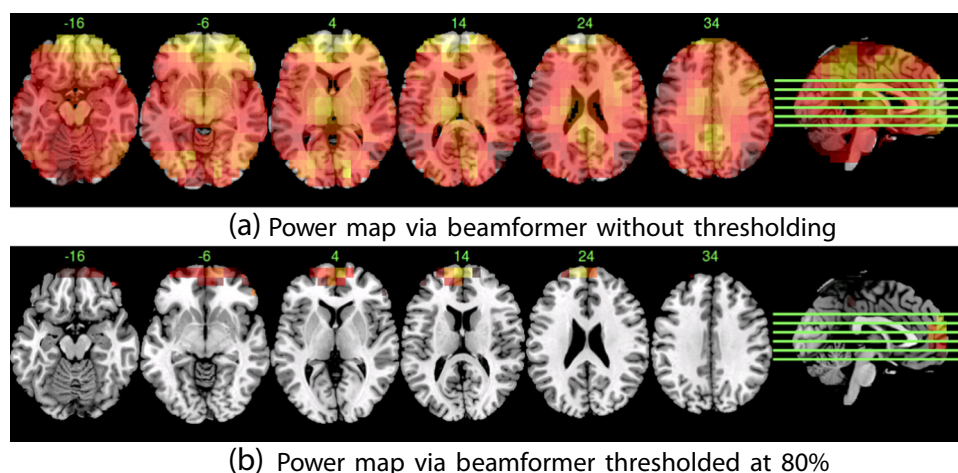


**Fig. 13.** Source imaging via beamforming and power mapping of the source-space of VEPs. The power of the voxels was measured over a window of 0–300 ms post-stimulus. Figure (a) shows the power map without thresholding whereas figure (b) shows the power map thresholded at 80%. The voxels in the frontal area had the highest power (due to ocular artifact) and therefore passed the thresholding.

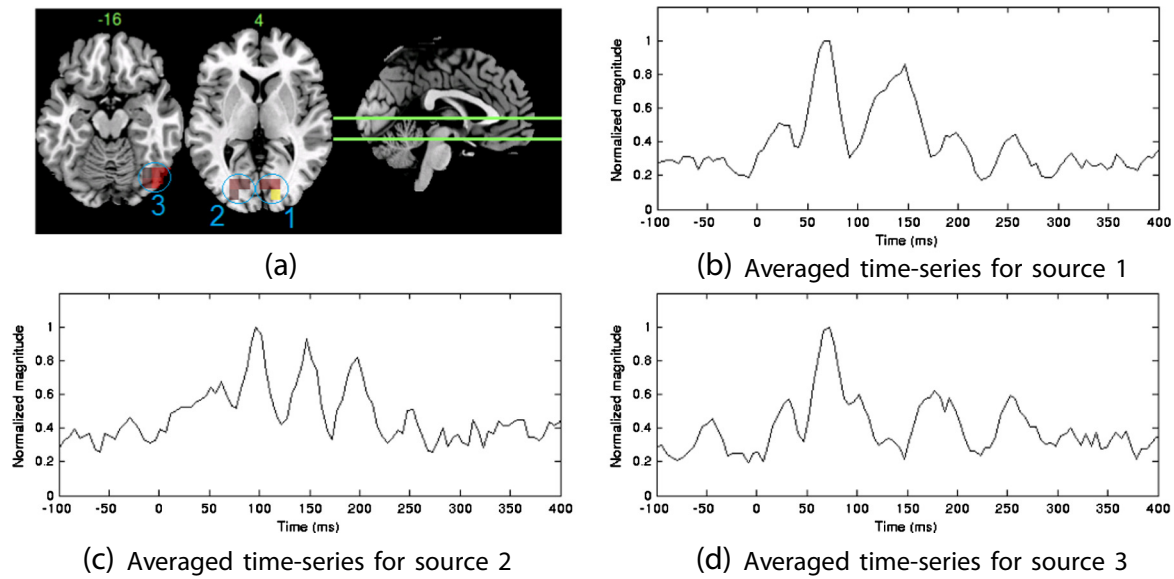


**Fig. 14.** (a) Source imaging of VEPs via beamforming and power of the source-space. After ocular artifact removal, the power of the voxels was measured, over a window of 0–300 ms post-stimulus, less pre-stimulus (–200–0 ms) power. Figures (b)–(d) show the time-courses of the 3 areas passing an 80% threshold.

a sharp tomographic map, whereas the power of the source-space measured by the beamformer shows that background activity is stronger than 8 of the 10 sources (Fig. 8e, below the red line).

Although we used the vector WNMV beamformer (Sekihara et al., 2001) to reconstruct the time-courses of voxels, other types of spatial filter (e.g., minimum-norm family) can also be used. The general

concept of source-space ICA in EEG (and MEG) is to apply SVD and ICA to the time-courses of the voxels, regardless of how the time-courses of the voxels have been reconstructed. However, the final result (e.g., spatial resolution and accuracy) will be dependent on the type of spatial filter used to reconstruct the time-courses. We chose the WNMV beamformer due to its normalized weight vectors and, hence,

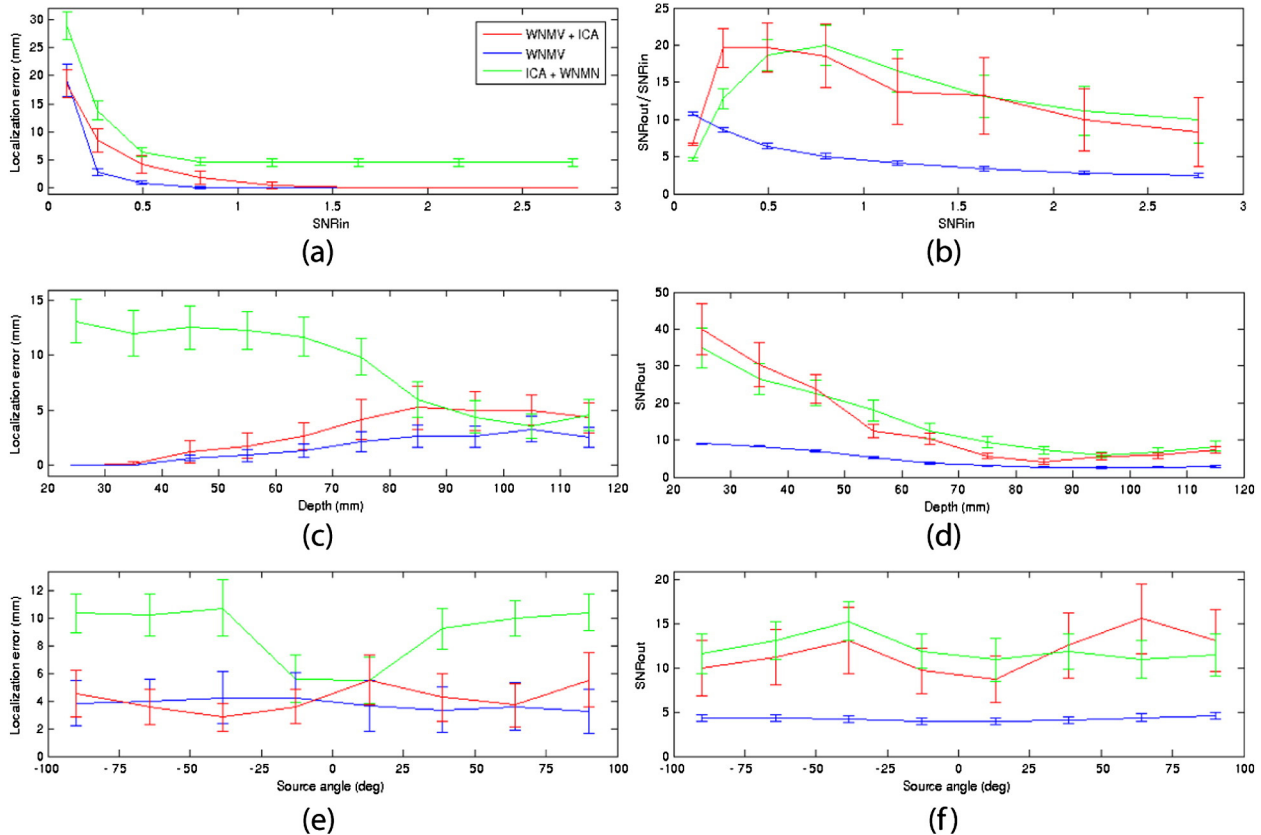


**Fig. 15.** Quantitative measurement of the localization error (left-side plots) and SNR (right-side plots) of a reconstructed source, with respect to changes in magnitude (figures (a) and (b)), depth (figures (c) and (d)), and orientation (figures (e) and (f)) of the simulated source. Three approaches were examined: (1) WNMV (blue), (2) WNMV + ICA (red), and (3) ICA + WNMN (green). The vertical bars are mean  $\pm$  95% confidence interval. For figure (b) the ratio of the SNR of the reconstructed source (SNRout) to the simulated source (SNRin) is shown. Depth was defined as the distance of the simulated source to a point on the scalp ( $[0 - 115 \ 0]$  mm). The source angle was the angle between the y vector and the simulated source. Figures (a) to (f) were obtained from 2160 simulations for each of the 3 approaches.

unit noise gain (uniform white-noise spatial map); that is, the time-courses of all voxels have the same gain (Greenblatt et al., 2005; Sekihara et al., 2005) and the non-uniform white noise spatial map which was shown in Van Veen et al. (1997) will not appear.

Similar to the options of different beamformers for source-space ICA, different BSS algorithms other than ICA can be considered as suitable variants of source-space ICA, such as spatio-spectral decomposition (Nikulin et al., 2011) and non-negative matrix factorization (Rutkowski et al., 2007). Each of these techniques has their own assumptions and, therefore, strengths and weaknesses. As there are options in both spatial filtering and BSS for the proposed approach, we consider source-space ICA to be a subcategory of the “source-space BSS” approach in EEG/MEG source imaging. Therefore, we propose “source-space BSS”, which includes source-space ICA, as a powerful alternative for EEG/MEG source imaging over the widely-used source-space power measurement.

The proposed source-space ICA is similar to the application of ICA in fMRI studies, with the main difference being that, for EEG and MEG, ICA is applied to the temporal subspace  $\mathbf{Y}$  whereas in the fMRI case, due to the poor temporal resolution of the voxel time-series, ICA is applied to the spatial subspace  $\mathbf{U}_D$  (e.g., Petersen et al. (2000) and Bai et al. (2008)). In the case of MEG, Brookes et al. (2011) (and similarly Luckhoo et al. (2012)) applied ICA in source-space, rather than sensor-space, for detection of the resting state brain networks. However, their approach is not generally applicable for source localization and time-reconstruction of brain sources, especially for highly transient neural sources, as in their approach the temporal resolution is considerably reduced due to enveloping and down-sampling of the voxel time-courses prior to application of ICA.

We carried out simulations to compare source-space ICA with other popular techniques in EEG source localization. However, there are other aspects in EEG which have not been considered in this study, such as rotating and moving (dynamic) sources, as the aim of this paper was to describe a new technique rather than undertake a comprehensive performance evaluation. In future work, we aim to evaluate the performance of source-space ICA under different conditions and also demonstrate its application in MEG source localization and reconstruction. The multiple simulations (Fig. 15) provided important information on localization error and quality of the reconstructed time-course via the different techniques. However, this did not show the main advantage of the two ICA approaches over beamforming by itself, as there was only one source (plus background activity) in all of the simulations, whereas multiple concurrent sources provide a greater challenge for the beamforming alone, as shown in the Multiple sources section. In the future, we also aim to compare source-space ICA with other techniques in such conditions.

In addition to being a valuable tool for separation, localization, and time-course reconstruction of sources, source-space ICA also has considerable potential as a step towards improved estimation of 3D functional connectivity in the brain. As source-space ICA reconstructs the time-series of each component separately, by applying techniques such as partial directed coherence to the time-series of these components it should be possible to better identify information flow and Granger causality between sources.

As source-space ICA performs analysis of EEG and/or MEG signals in the source-space (virtual sensors), it is similar to the other voxel-based brain imaging techniques such as fMRI, diffusion tensor imaging (DTI), and PET. Sui et al. (2011) performed fMRI and DTI data fusion via SVD, multimodal canonical correlation analysis (Correa et al., 2010), and joint-ICA (Calhoun et al., 2006) to discriminate between schizophrenia and bipolar disorder. Their approach has a similar structure to the proposed source-space ICA. They also mentioned that it is possible to perform EEG/MEG data fusion with fMRI, in which techniques such as joint-ICA can be applied to concatenated spatial maps of EEG ( $\mathbf{U}_D$  in this study) and fMRI or other imaging techniques. By changing its structure, it would also be possible to incorporate source-space ICA into the

fusion of information from EEG/MEG and other voxel-based brain imaging techniques.

### Conflict of interest

There is no conflict of interest.

### Acknowledgments

This work was supported by University of Otago, by way of a Postgraduate Scholarship, and by Marsden Fund (Grant VDV0801) by way of a Neurotechnology scholarship. The funding source did not have any role in the design or conduction of the study, collection, management, analysis, or interpretation of the data.

### Appendix A. Supplementary data

Supplementary data to this article can be found online at <http://dx.doi.org/10.1016/j.neuroimage.2014.07.052>.

### References

- Bai, P., Shen, H., Huang, X., Truong, Y., 2008. A supervised singular value decomposition for independent component analysis of fMRI. *Stat. Sin.* 18, 1233–1252.
- Bell, A.J., Sejnowski, T.J., 1995. An information-maximization approach to blind separation and blind deconvolution. *Neural Comput.* 7 (6), 1129–1159.
- Brookes, M.J., Woolrich, M., Luckhoo, H., Price, D., Hale, J.R., Stephenson, M.C., Barnes, G.R., Smith, S.M., Morris, P.G., 2011. Investigating the electrophysiological basis of resting state networks using magnetoencephalography. *Proc. Natl. Acad. Sci. U. S. A.* 108, 16783–16788.
- Bush, G., Luu, P., 2000. Cognitive and emotional influences in anterior cingulate cortex. *Trends Cogn. Sci.* 4, 215–222.
- Calhoun, V.D., Adali, T., Kiehl, K.A., Astur, R., Pekar, J.J., Pearlson, G.D., 2006. A method for multitask fMRI data fusion applied to schizophrenia. *Hum. Brain Mapp.* 27, 598–610.
- Cheyne, D., Bakhtazad, L., Gaetz, W., 2006. Spatiotemporal mapping of cortical activity accompanying voluntary movements using an event-related beamforming approach. *Hum. Brain Mapp.* 27, 213–229.
- Correa, N., Adali, T., Li, Y.O., Calhoun, V.D., 2010. Canonical correlation analysis for fusion and analysis of multi-modal medical imaging data. *IEEE Signal Proc. Mag.* 27, 39–50.
- Dale, A., Liu, A.K., Fischl, B.R., Buckner, R.L., Belliveau, J.W., Lewine, J.D., Halgren, E., 2000. Dynamic statistical parametric mapping: combining fMRI and MEG for high-resolution imaging of cortical activity. *Neuron* 26, 55–67.
- Delorme, A., Makeig, S., 2004. EEGLAB: an open source toolbox for analysis of single-trial EEG dynamics. *J. Neurosci. Methods* 134, 9–21.
- Fatima, Z., Quraan, M.A., Kovacevic, N., McIntosh, A., 2013. ICA-based artifact correction improves spatial localization of adaptive spatial filters in MEG. *NeuroImage* 78, 284–294.
- Greenblatt, R.E., Ossadtchi, A., Pflieger, M.E., 2005. Local linear estimators for the linear bioelectromagnetic inverse problem. *IEEE Trans. Biomed. Eng.* 53 (9), 3403–3412.
- Hämäläinen, M.S., Ilmoniemi, R.J., 1994. Interpreting magnetic fields of the brain: minimum norm estimates. *Med. Biol. Eng. Comput.* 32, 35–42.
- Huang, M.X., Shih, J.J., Lee, R.R., Harrington, D.L., Thoma, R.J., Weisend, M.P., Hanlon, F., Paulson, K.M., Li, T., Martin, K., Millers, G.A., Canive, J.M., 2004. Commonalities and differences among vectorized beamformers in electromagnetic source imaging. *Brain Topogr.* 16 (3), 139–158.
- Jervis, B., Belal, S., Camilleri, K., Cassar, T., Bigan, C., Linden, D., Michalopoulos, K., Zervakis, M., Besleaga, M., Fabri, S., Muscat, J., 2007. The independent components of auditory P300 and CNV evoked potentials derived from single-trial recordings. *Physiol. Meas.* 28, 745–771.
- Jonmohamadi, Y., Poudel, G., Innes, C., Jones, R., 2013. Electromagnetic tomography via source-space ICA. *Proc. Int. Conf. IEEE Eng. Med. Biol. Soc.* 35, 37–40.
- Jonmohamadi, Y., Poudel, P., Poudel, G., Innes, C., Jones, R., 2014b. Voxel-ICA for reconstruction of source signal time-series and orientation in EEG and MEG. *Australas. Phys. Eng. Sci. Med.* 37, 457–464.
- Jung, T.P., Humphries, C., Lee, T.W., Makeig, S., McKeown, M.J., Iragui, V., Sejnowski, T.J., 1998. Extended ICA removes artifacts from electroencephalographic recordings. *Adv. Neural Inf. Process. Syst.* 10, 894–900.
- Jung, T.P., Makeig, S., Humphries, C., Lee, T.W., McKeown, M.J., Iragui, V., Sejnowski, T.J., 2000. Removing electroencephalographic artifacts by blind source separation. *Psychophysiology* 37, 163–178.
- La Foresta, F., Mammone, N., Morabito, F., 2009. PCAICA for automatic identification of critical events in continuous coma-EEG monitoring. *Biomed. Signal Process. Control* 4, 229–235.
- Luckhoo, H., Hale, J.R., Stokes, M.G., Nobre, A.C., Morris, P.G., Brookes, M.J., Woolrich, M.V., 2012. Inferring task-related networks using independent component analysis in magnetoencephalography. *NeuroImage* 62, 530–541.
- Makeig, S., Debener, S., Onton, J., Delorme, A., 2004. Mining event-related brain dynamics. *Trends Cogn. Sci.* 8, 204–210.

- Jonmohamadi, Y., Krueger, R., Weiss, D., Poudel, G., Innes, C., Jones, R., 2014. Comparison of beamformers for EEG source signal reconstruction. *Biomed. Signal Process, Control*, <http://dx.doi.org/10.1016/j.bspc.2014.07.014>.
- Mosher, J.C., Lewis, P.S., Leahy, R.M., 1992. Multiple dipole modeling and localization from spatio-temporal MEG data. *IEEE Trans. Biomed. Eng.* 39, 541–557.
- Nikulin, V.V., Nolte, G., Curio, G., 2011. A novel method for reliable and fast extraction of neuronal EEG/MEG oscillations on the basis of spatio-spectral decomposition. *NeuroImage* 55, 1528–1535.
- Onton, J., Westerfield, M., Townsend, J., Makeig, S., 2006. Imaging human EEG dynamics using independent component analysis. *Neurosci. Biobehav. Rev.* 30, 808–822.
- Oostendorp, T.F., van Oosterom, A., 1989. Source parameter estimation in inhomogeneous volume conductors of arbitrary shape. *IEEE Trans. Biomed. Eng.* 36, 382–391.
- Oostenveld, R., Fries, P., Maris, E., Schoffelen, J.M., 2011. Fieldtrip: open source software for advanced analysis of MEG, EEG, and invasive electrophysiological data. *Comput. Intell. Neurosci.* 2011, 1–9.
- Owen, J.P., Wipf, D.P., Attias, H.T., Sekihara, K., Nagarajan, S.S., 2012. Performance evaluation of the Champagne source reconstruction algorithm on simulated and real M/EEG data. *Neuroscience* 60 (1), 305–323.
- Pascual-Marqui, R.D., 2002. Standardized low-resolution brain electromagnetic tomography (sLORETA): technical details. *Methods Find. Exp. Clin. Pharmacol.* 24 (Suppl. D), 5–12.
- Petersen, K.S., Hansen, L.K., Kolenda, T., Rostrup, E., Strother, S.C., 2000. On the independent components of functional neuroimages. *Proc 3rd Int. Conf. Independent Component Analysis and Blind Source Separation (ICA 2000)*, pp. 615–620.
- Quraan, M.A., Cheyne, D., 2010. Reconstruction of correlated brain activity with adaptive spatial filters in MEG. *NeuroImage* 49, 2387–2400.
- Robinson, S.E., 2004. Localization of event-related activity by SAM(erf). *Neuro. Clin. Neurophysiol.* 2004, 109.
- Robinson, S.E., Vrba, J., 1998. Functional neuroimaging by synthetic aperture magnetometry (SAM). In: Yoshimoto, T., Kotani, M., Kuriki, S., Karibe, H., Nakasato, N. (Eds.), *Proc. 11th Int. Conf. Biomagnetism*. Tohoku Univ. Press, Sendai, pp. 302–305.
- Rossion, B., Jacques, C., 2012. The N170: understanding the time course of face perception in the human brain. In: Kappenman, E.S., Luck, S.J. (Eds.), *The Oxford Handbook of Event-related Potential Components*. Oxford University Press, New York.
- Rutkowski, T.M., Zdunek, R., Cichocki, A., 2007. Multichannel EEG brain activity pattern analysis in time–frequency domain with nonnegative matrix factorization support. *Int. Congr. Ser.* 1301, 266–269.
- Sanei, S., Chambers, J.A., 2007. *EEG Signal Processing*. John Wiley & Sons, LTD, Chichester, West Sussex.
- Sarvas, J., 1987. Basic mathematical and electromagnetic concepts of the biomagnetic inverse problem. *Phys. Med. Biol.* 32, 11–22.
- Sekihara, K., Nagarajan, S.S., 2008. *Adaptive Spatial Filters for Electromagnetic Brain Imaging*. Springer, Berlin.
- Sekihara, K., Nagarajan, S.S., Poeppel, D., Marantz, A., Miyashita, Y., 2001. Reconstructing spatio-temporal activities of neural sources using an MEG vector beamformer technique. *IEEE Trans. Biomed. Eng.* 48 (7), 760–771.
- Sekihara, K., Sahani, M., Nagarajan, S.S., 2005. Localization bias and spatial resolution of adaptive and non-adaptive spatial filters for MEG source reconstruction. *NeuroImage* 25, 1056–1067.
- Sui, J., Pearson, G., Caprihan, A., Adali, T., Kiehl, K.A., Liu, J., Yamamoto, J., Calhoun, V.D., 2011. Discriminating schizophrenia and bipolar disorder by fusing fMRI and DTI in a multi-modal CCA + joint ICA model. *NeuroImage* 57, 839–855.
- Uutela, K., Hämäläinen, M.S., Salmelin, R., 1983. Global optimization in the localization of neuromagnetic sources. *IEEE Trans. Biomed. Eng.* 45, 716–723.
- Van Veen, B.D., van Drongelen, W., Yuchtman, M., Suzuki, A., 1997. Localization of brain electrical activity via linearly constrained minimum variance spatial filtering. *IEEE Trans. Biomed. Eng.* 44 (9), 867–880.
- Ventouras, E.M., Ktonas, P.Y., Tsekou, H., Paparrigopoulos, T., Kalatzis, I., Soldatos, C.R., 2010. Independent component analysis for source localization of EEG sleep spindle components. *Comput. Intell. Neurosci.* 2010, 1–12.
- Wipf, D.P., Owen, J.P., Attias, H.T., Sekihara, K., Nagarajan, S.S., 2009. Estimating the location and orientation of complex, correlated neural activity using MEG. *Inf. Process. Syst.* 21, 1777–1784.
- Wipf, D.P., Owen, J.P., Attias, H.T., Sekihara, K., Nagarajan, S.S., 2010. Robust Bayesian estimation of the location, orientation, and time course of multiple correlated neural sources using MEG. *NeuroImage* 21, 641–655.